Resonant-plane locking and spin alignment in stellar-mass black-hole binaries: A diagnostic of compact-binary formation

Davide Gerosa, Michael Kesden, Emanuele Berti, Richard O'Shaughnessy, and Ulrich Sperhake

Phys. Rev. D **87**, 104028 — Published 22 May 2013

DOI: 10.1103/PhysRevD.87.104028

Resonant-plane locking and spin alignment in stellar-mass black-hole binaries: a diagnostic of compact-binary formation

Davide Gerosa,[1, 2, *] Michael Kesden,[3, †] Emanuele Berti,[1, 4, ‡]
Richard O'Shaughnessy,[5, §] and Ulrich Sperhake[6, 1, 4, 7, ¶]

[1] *Department of Physics and Astronomy, The University of Mississippi, University, MS 38677, USA*
[2] *Dipartimento di Fisica, Universitá Degli Studi di Milano, Via Celoria, 16, Milano, 20133, Italy*
[3] *Center for Cosmology and Particle Physics, New York University, 4 Washington Pl., New York, NY 10003, USA*
[4] *California Institute of Technology, Pasadena, CA 91109, USA*
[5] *Center for Gravitation and Cosmology, University of Wisconsin-Milwaukee, Milwaukee, WI 53211, USA*
[6] *Department of Applied Mathematics and Theoretical Physics, Centre for Mathematical Sciences, University of Cambridge, Wilberforce Road, Cambridge CB3 0WA, UK*
[7] *Centro Multidisciplinar de Astrofísica – CENTRA, Departamento de Física, Instituto Superior Técnico – IST, 1049-001 Lisboa, Portugal*

(Dated: April 26, 2013)

We study the influence of astrophysical formation scenarios on the precessional dynamics of spinning black-hole binaries by the time they enter the observational window of second- and third-generation gravitational-wave detectors, such as Advanced LIGO/Virgo, LIGO-India, KAGRA and the Einstein Telescope. Under the plausible assumption that tidal interactions are efficient at aligning the spins of few-solar mass black-hole progenitors with the orbital angular momentum, we find that black-hole spins should be expected to preferentially lie in a plane when they become detectable by gravitational-wave interferometers. This "resonant plane" is identified by the conditions $\Delta\Phi = 0^\circ$ or $\Delta\Phi = \pm 180^\circ$, where $\Delta\Phi$ is the angle between the components of the black-hole spins in the plane orthogonal to the orbital angular momentum. If the angles $\Delta\Phi$ can be accurately measured for a large sample of gravitational-wave detections, their distribution will constrain models of compact binary formation. In particular, it will tell us whether tidal interactions are efficient and whether a mechanism such as mass transfer, stellar winds, or supernovae can induce a mass-ratio reversal (so that the heavier black hole is produced by the initially lighter stellar progenitor). Therefore our model offers a concrete observational link between gravitational-wave measurements and astrophysics. We also hope that it will stimulate further studies of precessional dynamics, gravitational-wave template placement and parameter estimation for binaries locked in the resonant plane.

PACS numbers: 04.25.dg, 04.70.Bw, 04.30.-w

I. INTRODUCTION

The inspiral and merger of stellar-mass black-hole (BH) binaries is one of the main targets of the future network of second-generation gravitational-wave (GW) interferometers (including Advanced LIGO/Virgo [1], LIGO-India [2] and KAGRA [3]) and of third-generation interferometers, such as the proposed Einstein Telescope [4]. Typical GW signals from these binaries are expected to have low signal-to-noise ratios, and must therefore be extracted by matched filtering, which consists of computing the cross-correlation between the noisy detector output and a predicted theoretical waveform, or template (see e.g. [5]). The number of observationally distinguishable merger signals should be extremely large, both because of the large and strongly mass-dependent number of cycles in each signal and because the emitted waveform depends sensitively on as many as 17 different parameters, in the general case where the BHs are spinning and in eccentric orbits. The difficult task of exploring such a high-dimensional space can be simplified if nature provides physical mechanisms that cause astrophysical binaries to cluster in restricted portions of the parameter space.

In this paper we consider one mechanism to preferentially populate certain regions of parameter space: the post-Newtonian (PN) spin-orbit resonances first discovered by Schnittman [6]. Unfortunately, very few of the existing population-synthesis models of compact-binary formation (see e.g. [7, 8]) include self-consistent predictions for BH spins. To highlight the significance of spin-orbit misalignment and resonances, we adopt a simplified model for binary BH formation. We use this model to generate initial conditions for our compact binaries, and then integrate the PN equations of motion forward in time using an extension of the code used by some of us in previous studies of supermassive BH binaries [9–11]. Our analytically tractable model captures (at least qualitatively) many of the detailed physical effects influencing the evolution of BH spins. Within this framework we carry out Monte Carlo simulations to study the statis-

* dgerosa@olemiss.edu
† mhk10@nyu.edu
‡ berti@phy.olemiss.edu
§ oshaughn@gravity.phys.uwm.edu
¶ sperhake@tapir.caltech.edu

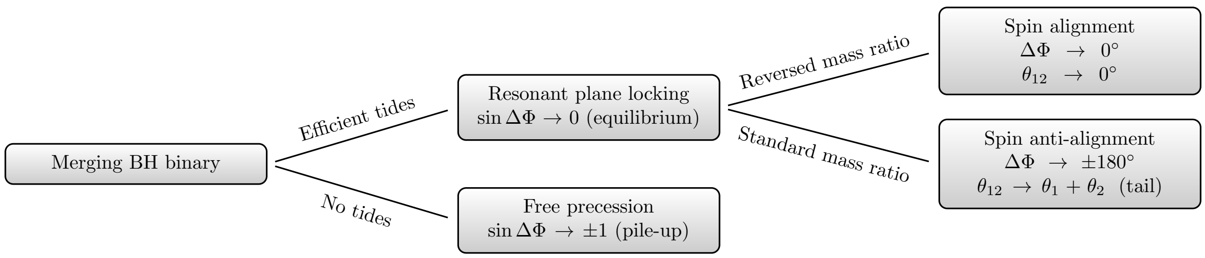

FIG. 1. Schematic summary of our predictions for the spin orientation of BH binaries as they enter the LIGO/Virgo band. If tides efficiently align the spin of the secondary with the orbital angular momentum prior to the second supernova, resonant-plane locking will drive $\sin\Delta\Phi \to 0$, while in the absence of tides the spins will precess freely, piling up around $\sin\Delta\Phi \to \pm 1$ near merger. When tides are efficient, if the primary star evolves into the less massive BH (reversed mass ratio) the PN evolution will drive $\Delta\Phi \to 0^\circ, \theta_{12} \to 0^\circ$. If instead the primary star evolves into the more massive BH (standard mass ratio) the PN evolution will drive $\Delta\Phi \to \pm 180^\circ, \theta_{12} \to \theta_1 + \theta_2$, generating a tail in the distribution of θ_{12} to larger values. See Eqs. (2) and (3) for definitions of these angles.

tical distribution of BH spins when they enter the GW-detection band of second- and third-generation detectors.

Before summarizing our results, we first introduce some notation. Consider a BH binary with component masses $m_1 \geq m_2$, total mass $M = m_1 + m_2$ and mass ratio $q = m_2/m_1 \leq 1$. The spin $\mathbf{S_i}$ of each BH can be written as

$$\mathbf{S_i} = \chi_i \frac{G m_i^2}{c} \mathbf{\hat{S}_i}\,, \tag{1}$$

where $0 \leq \chi_i \leq 1$ $(i = 1, 2)$ is the dimensionless spin magnitude and a hat denotes a unit vector. Our goal is not to rival the complexity of existing population-synthesis models of compact-binary formation, but rather to investigate specifically those astrophysical ingredients which affect the spin dynamics. We therefore focus on maximally spinning BH binaries with mass ratio $q = 0.8$, a typical value predicted by population-synthesis studies (cf. e.g. Fig. 9 of [12]).

Let us define θ_i to be the angle between each spin $\mathbf{S_i}$ and the orbital angular momentum of the binary $\mathbf{L}$, θ_{12} to be the angle between $\mathbf{S_1}$ and $\mathbf{S_2}$, and $\Delta\Phi$ to be the angle between the projection of the spins on the orbital plane:

$$\cos\theta_1 = \mathbf{\hat{S}_1} \cdot \mathbf{\hat{L}}, \qquad \cos\theta_2 = \mathbf{\hat{S}_2} \cdot \mathbf{\hat{L}}, \tag{2}$$

$$\cos\theta_{12} = \mathbf{\hat{S}_1} \cdot \mathbf{\hat{S}_2}, \quad \cos\Delta\Phi = \frac{\mathbf{\hat{S}_1} \times \mathbf{\hat{L}}}{|\mathbf{\hat{S}_1} \times \mathbf{\hat{L}}|} \cdot \frac{\mathbf{\hat{S}_2} \times \mathbf{\hat{L}}}{|\mathbf{\hat{S}_2} \times \mathbf{\hat{L}}|}. \tag{3}$$

As we will demonstrate below, the physical mechanisms leading to the formation of the BH binary leave a characteristic imprint on the angles $\Delta\Phi$ and θ_{12}. This has implications for GW data analysis and, even more strikingly, for GW astronomy: at least in principle, measurements of spin orientation with future GW detections can constrain the astrophysical evolutionary processes that lead the binary to merger.

All BH binaries with misaligned spins ($\theta_i \neq 0$) experience PN spin precession as they inspiral towards merger. Although ensembles of BH binaries with isotropic spin distributions retain their isotropic distributions as they inspiral [13], anisotropic spin distributions can be substantially affected by PN spin precession [6]. In particular, binaries can be attracted towards PN spin-orbit resonances in which the BH spins and orbital angular momentum jointly precess in a common plane ("resonant-plane locking"). Binaries in which the two BH spins and the orbital angular momentum do not share a common plane at the end of the inspiral are said to precess freely. Binaries can become locked into resonance if they satisfy the following conditions at large separations:

i) comparable but not equal masses ($0.4 \lesssim q \neq 1$),

ii) sufficiently large spin magnitudes ($\chi_i \gtrsim 0.5$),

iii) unequal spin misalignments ($\theta_1 \neq \theta_2$).

If these conditions are satisfied, the spin distribution of an ensemble of binaries will be strongly influenced by the PN resonances although every individual member of the ensemble will not necessarily become locked into resonance. In ensembles of binaries for which $\theta_1 < \theta_2$ at large separations, the two spins tend to align with each other, so that $\Delta\Phi \to 0^\circ$, $\theta_{12} \to 0^\circ$. If instead $\theta_1 > \theta_2$, the projections of the BH spins on the orbital plane tend to anti-align, so that $\Delta\Phi \to 180^\circ, \theta_{12} \to \theta_1 + \theta_2$. The mass ratios for which resonant-plane locking is effective, given by condition i) above, are typical for the stellar-mass BH binaries detectable by Advanced LIGO/Virgo (cf. Fig. 9 of [12]). The spin magnitudes χ_i of newly formed BHs are highly uncertain, but observations of accreting BHs in binary systems indicate that their spins span the whole range $0 \leq \chi_i \leq 1$ allowed by general relativity [14, 15]. Many BH-BH systems may therefore satisfy condition ii) above. In contrast, we would not expect resonance locking in binaries in which one or both members are neutron stars, as they are expected to have small spins[1]. Whether the spin misalignments of the ensemble of BH binaries detectable by Advanced LIGO/Virgo is asymmetric (satisfying condition iii) above) is a primary consideration of this paper.

Astrophysical formation channels determine the initial conditions for PN evolutions in the late inspiral. As a result they determine whether resonant locking can occur, and which resonant configuration is favored. Here we introduce a model for BH binary formation that allows us to establish a link between binary-formation channels and the near-merger spin configurations of precessing BH binaries.

A. Executive summary

Our main findings are summarized schematically in Fig. 1. Supernova (SN) kicks tilt the orbit, producing a misalignment between the orbital angular momentum and the orientation of the spins of the binary members [25]. As a result, the main factors determining the spin alignment of a BH binary are the magnitude of SN kicks and the possibility that other physical effects may realign the spins with the orbital angular momentum in between SN events. Dominant among these physical effects (aside from the SN kick itself) are the efficiency of tidal interactions and the possibility of a mass-ratio reversal due to mass transfer from the initially more massive, faster evolving progenitor.

Tides affect the binary in two significant ways: they align the spins of stellar BH progenitors with the orbital angular momentum and they reduce the binary eccentricity. Additionally, tides force stars to rotate synchronously with the orbit, increasing the likelihood of a large BH spin at collapse and implying that our results will depend only mildly (if at all) on the initial stellar spin. Consider the evolution of the system between the two SN events, when the binary consists of a BH and a non-degenerate star. If tidal interactions are efficient (a reasonable assumption, as we argue in Appendix A 6) they tend to align the star (but not the BH) with the orbital angular momentum. This introduces an asymmetry in the angles (θ_1, θ_2) which is critical to determining the spin configuration at the end of the inspiral.

Mass transfer can change the mass ratio of interacting binaries. Since the main-sequence lifetime of a star is a decreasing function of its mass, the initially more massive star in a binary is expected to collapse first. If mass transfer from this star to its less massive companion is insufficient, which we will refer to as the *standard mass ratio* (SMR) scenario, the initially more massive star will go on to form the more massive member of the BH binary. We cannot however rule out the possibility that prior to the first SN, the initially more massive star overflows its Roche lobe and donates mass to its initially lighter, longer-lived companion. This mass transfer may produce a mass-ratio reversal, so that the heavier BH in the binary forms second: we will call this the *reversed mass ratio* (RMR) scenario. According to population-synthesis models, mass-ratio reversal happens for a sizable fraction (typically from $\sim 10\%$ to 50%) of the total number of BH binaries (cf. [12] and Table III below).

Since BHs are relatively immune to the effects of tides, the spin of the first BH to form will be more misaligned than the spin of the second BH, as this misalignment will have accumulated due to the kicks generated during *both* SN events. Therefore, in the SMR scenario BH binaries will have $\theta_1 > \theta_2$ at formation, and thus $\Delta\Phi \simeq \pm 180°$ by the time they enter the GW-detection band. On the other hand, in the RMR scenario BH binaries initially have $\theta_1 < \theta_2$, so that by late in the inspiral $\Delta\Phi \simeq \pm 0°$, and furthermore the spins are nearly aligned with each other (i.e., $\theta_{12} \simeq 0$). In summary, whenever tidal interactions are efficient, our model predicts that BH spins should preferentially lie in a "resonant plane" (identified by the conditions $\Delta\Phi = 0°$ in the RMR scenario, and $\Delta\Phi = \pm 180°$ in the SMR scenario) when they become detectable by GW interferometers.

A third (more unlikely) possibility is that tidal interactions are not efficient. In this case, binaries form with $\theta_1 \simeq \theta_2$ and will not become locked into resonant configurations. Our simulations show that binaries will preferentially have $\Delta\Phi \simeq \pm 90°$. Because the most likely values of $\Delta\Phi$ in the three scenarios (RMR, SMR and no tides) are mutually exclusive, GW measurements of a statistically significant sample of values of $\Delta\Phi$ will provide important astrophysical information on compact-binary formation scenarios. In particular, they will tell us whether tidal interactions are efficient, and (if so) whether mass transfer can produce mass-ratio reversals.

Fig. 2 makes these conclusions more quantitative by showing three histograms of $\Delta\Phi$ (left) and θ_{12} (right), corresponding to snapshots taken at different times during the inspiral. The distribution of $\Delta\Phi$ is flat at large separations (dotted lines, corresponding to early times and small orbital frequency) because spin-spin couplings are weak, and the BH spins simply precess about the orbital angular momentum. If tidal alignment is efficient, in the late inspiral the BH spins lock into equilibrium configurations with either $\Delta\Phi = 0°$ or $\Delta\Phi = \pm 180°$. This effect is clearly visible at GW frequencies $f_{\rm GW} = 1$ Hz, roughly corresponding to the lowest cutoff frequency of third-generation detectors like ET, and it is even more pronounced when the binaries enter the Ad-

[1] Relativistic calculations of neutron star structure suggest that $\chi_i \lesssim 0.7$ for uniform rotation and physically motivated equations of state [16–18], but the spin magnitudes of neutron stars in binaries observable by Advanced LIGO are likely to be much smaller than this theoretical upper bound [19, 20]. The spin period of isolated neutron stars at birth should be in the range 10-140 ms [21], or $\chi_i \lesssim 0.04$. Accretion from a binary companion can spin up neutron stars but is unlikely to produce periods less than 1 ms, i.e. $\chi_i \lesssim 0.4$ [22]. The fastest-spinning observed pulsar has a period of 1.4 ms, ($\chi_i \sim 0.3$) [23]; the fastest known pulsar in a neutron star-neutron star system, J0737-3039A, has a period of 22.70 ms ($\chi_i \sim 0.02$) [24].

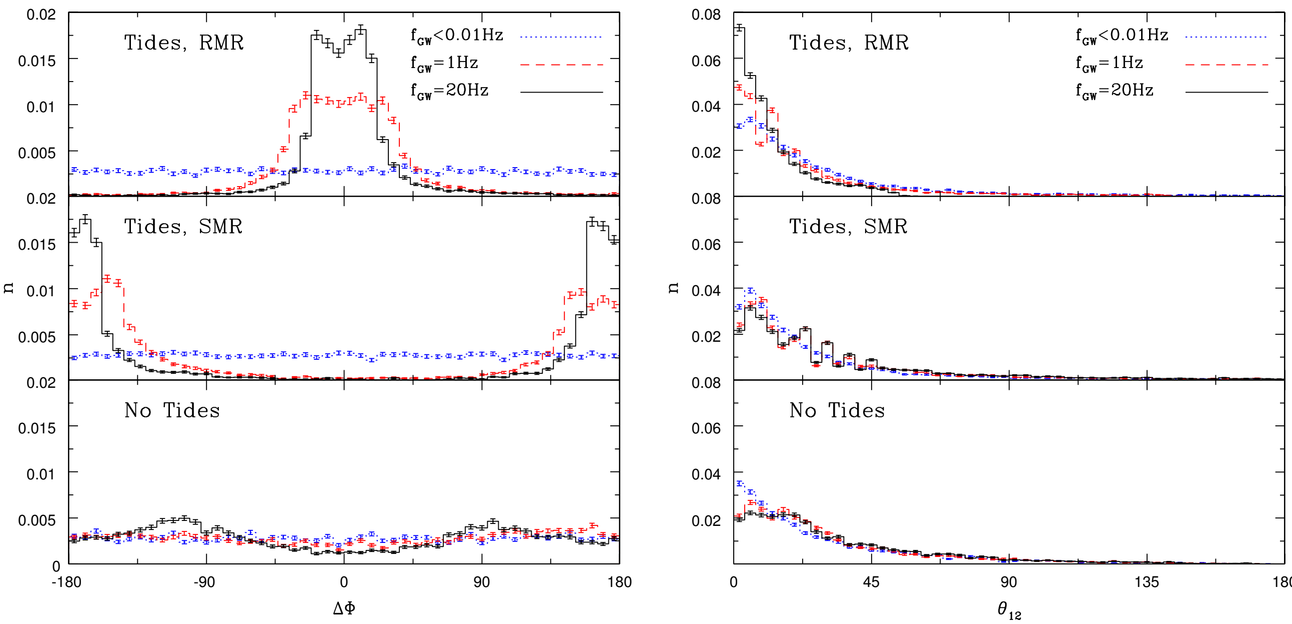

FIG. 2. (Color online.) Left: Probability distribution of the angle between the projections of the spins on the orbital plane $\Delta\Phi$. As the binaries inspiral, the GW frequency $f_{\rm GW}$ increases from 0.01 Hz (dotted blue lines) to 1 Hz (dashed red lines) and later 20 Hz (solid black lines). Under the effect of tides the PN evolution brings the spins in the same plane ($\Delta\Phi \to 0^\circ, \pm 180^\circ$), both in a reversed mass ratio (RMR, top panel) and in a standard mass ratio (SMR, middle panel) scenario. When tidal effects are removed (bottom panel, where we show both RMR and SMR binaries) the spins precess freely and pile up at $\Delta\Phi = \pm 90^\circ$. Right: Probability distribution of the angle between the two spins θ_{12}. In the RMR scenario (top panel) the spins end up almost completely aligned with each other, i.e. most binaries have $\theta_{12} \simeq 0^\circ$. In the SMR scenario (middle panel) and in the absence of tides (bottom panel, where again we show both RMR and SMR binaries) a long tail at large values of θ_{12} remains even in the late inspiral. All simulations shown in this figure assume that kick directions are isotropically distributed. Error bars are computed assuming statistical Poisson noise.

vanced LIGO/Virgo band at $f_{\rm GW} \simeq 20$ Hz. If tides are artificially removed, free precession during the late stages of the inspiral slows down the evolution of $\Delta\Phi$ when the components of the spin orthogonal to the orbital angular momentum are also orthogonal to each other, causing binaries that are not locked into resonance to pile up at $\Delta\Phi = \pm 90^\circ$.

Let us stress again that the statistical effect of resonances is clearly visible at $f_{\rm GW} = 20\,$Hz, i.e. when BH binaries enter the Advanced LIGO/Virgo band. GW measurements of $\Delta\Phi$ can therefore be used to constrain uncertainties in BH binary-formation scenarios. The inclusion of resonant effects in population-synthesis models (combined with a statistically significant sample of GW measurements of $\Delta\Phi$) has the potential to constrain various aspects of the models, such as the efficiency of tides, stable mass transfer, common-envelope (CE) evolution, SN kick velocities, and the metallicity of BH progenitors.

B. Outline of the paper

The rest of the paper provides details of our astrophysical model and a more detailed discussion of the results. In Section II we introduce our fiducial BH binary-formation channels, which are based on detailed population-synthesis models, as described at much greater length in Appendix A. In order to focus on spin effects, we fix the component masses to two representative values. We assume that SN kicks follow a Maxwellian distribution in magnitude. We also assume that the kicks are distributed in a double cone of opening angle θ_b about the spin of the exploding star and, to bracket uncertainties, we consider two extreme scenarios: isotropic ($\theta_b = 90^\circ$) or polar ($\theta_b = 10^\circ$) kicks.

Section III summarizes the results of evolving these BH binaries under the effect of gravitational radiation down to a final separation of $10GM/c^2$. We demonstrate that spin-orbit resonances have a significant impact on the observable properties of our fiducial BH binaries. Although we have only explored a handful of evolutionary channels and component masses, in Section IV we argue that the scenarios described in Fig. 1 are broadly applicable: kicks, tides, and the mass-ratio distribution control spin alignment. We explore the sensitivity of these three features (and hence of the observable distribution of resonantly-locked binaries) to several poorly constrained physical inputs to binary-evolution models, and we argue that GW observations of precession angles could provide significant constraints on binary formation channels. Finally, in Section V we describe the implications of our results for future efforts in binary-evolution modeling and GW detection.

To complement and justify the simple astrophysical model proposed in Section II, in Appendix A we describe in detail the rationale underlying the model and its relationship to our current understanding of binary evolution. Appendix A should provide a useful resource to implement (and possibly improve) the Monte-Carlo algorithm described in the main text.

II. ASTROPHYSICAL MODEL OF THE INITIAL CONDITIONS FOR SPIN EVOLUTION

Isolated BH binaries do not emit electromagnetically and hence have yet to be observed. Despite this lack of evidence, they are a likely outcome of the evolution of massive stellar binaries. The rate at which they form can be inferred from observations of their progenitors and systems like binary neutron stars that have similar formation channels. Formation rates can also be calculated theoretically using population-synthesis models such as `StarTrack` [12, 26–28], which builds upon previous analytical studies of single [29] and binary stellar evolution [30].

Most studies of compact-binary formation do not keep track of the magnitude and orientation of BH spins, and those that do (see e.g. [7, 8, 31]) neglect general-relativistic effects in the late-time evolution of the binary. One of the goals of our study is to fill this gap. For example, the version of the `StarTrack` code used in [7] assumed that both $\mathbf{S_1}$ and $\mathbf{S_2}$ remained aligned with the initial direction of the orbital angular momentum $\mathbf{L}$. The evolution of $\mathbf{L}$ itself was performed by applying energy and angular-momentum conservation when compact objects are formed (and kicked) as a result of gravitational collapse. This approach is suitable for binaries in non-relativistic orbits, like observed X-ray binaries [8, 31], but it may not be appropriate for merging binaries, that are interesting both as GW sources and as progenitors of short gamma-ray bursts [7]. Since existing BH binary-formation models preserve the mutual alignment of the spins with the initial direction of $\mathbf{L}$, all BH-BH binaries are formed with $\theta_1 = \theta_2$. Later models of mixed BH X-ray binaries do allow for the possibility of asymmetric spin configurations via accretion [8], but to the best of our knowledge no such studies have been published for the BH-BH case. Since PN resonance locking only occurs when $\theta_1 \neq \theta_2$, its effects are excluded by construction in the BH binary models available in the literature.

Here we develop a slightly more complex (and presumably more realistic) model for spin evolution, allowing for the formation of "asymmetric" BH binaries with $\theta_1 \neq \theta_2$. The model is not meant to rival the complexity of population-synthesis codes like `StarTrack`. Our goal is rather to isolate the physical ingredients that are specifically relevant to BH spin alignment. The model builds, when necessary (e.g. when computing the remnant masses resulting from gravitational collapse as a function of the progenitor masses, or in treating the CE phase) on results from `StarTrack`, and in Section IV we present a preliminary comparison of our conclusions with publicly available results from `StarTrack`.

A. Length scales

Before describing our astrophysical model, we review the length scales associated with the formation, inspiral, and merger of BH binaries. The well defined hierarchy in these length scales demonstrates the necessity of our joint analysis of astrophysics and PN evolution. GW emission [32, 33] causes a binary with a semimajor axis less than

$$a_{\rm H} \sim 45 \left[\frac{q}{(1+q)^2} \left(\frac{t_{\rm GW}}{10^{10}\ {\rm yrs}} \right) \left(\frac{M}{10 M_\odot} \right)^3 \right]^{1/4} R_\odot \quad (4)$$

to merge on a timescale $t_{\rm GW}$ less than the Hubble time $t_{\rm H} \simeq 10^{10}$yrs. The astrophysical processes described in this Section, including mass transfer, SN explosions[2] and CE evolution, are required to shrink the binary down to separations smaller than $a_{\rm H}$. GW emission also circularizes the binary at separations comparable to $a_{\rm H}$. PN spin-orbit couplings become important at much smaller separations

$$a_{\rm PNi} \sim 10^3 \frac{GM}{c^2} \simeq 10^{-2} \left(\frac{M}{10 M_\odot} \right) R_\odot \,, \quad (5)$$

below which they can lock binaries into resonant configurations with well defined spin directions [6]. Previous studies of PN resonances for supermassive BHs [9–11] found that the effectiveness of resonance locking strongly depends on the orientation of the BH spins when the binary reaches the separation $a_{\rm PNi}$. The spin orientation is set by the binary's astrophysical formation history. Resonance locking can be important even at separations above

$$a_{\rm LIGO} \simeq 10^{-3} \left(\frac{M}{10 M_\odot} \right)^{1/3} \left(\frac{f_{\rm GW}}{20 {\rm Hz}} \right)^{-2/3} R_\odot \,, \quad (6)$$

at which the binary reaches the lower limit $f_{\rm GW} \simeq 10-20$ Hz of the Advanced LIGO/Virgo sensitivity band. The third-generation Einstein Telescope is expected to reach even lower frequencies of order $f_{\rm GW} \simeq 1$ Hz. Since these frequencies are well within the regime where PN resonances are important, a unified treatment of the astrophysical initial conditions and of the subsequent PN

[2] Throughout the paper we will loosely use the term "supernova" to indicate the core collapse of massive stars, even when such events are not luminous.

evolution of the binary is essential to determining which spin configurations are most relevant for GW detectors. Such a treatment is the main goal of this work.

B. Fiducial scenarios for binary evolution

In this Section we describe how massive main-sequence binary stars evolve into BH binaries. Fig. 3 summarizes the critical stages of binary evolution in our model. To isolate the effects of spin orientation during the PN inspiral of the BH binaries, we fix the final mass ratio to the typical value $q = 0.8$ [12]. To ensure that this final mass ratio is obtained, the initial stellar masses of the binaries must be fixed to $(M'_{Si}, M''_{Si}) = (35M_\odot, 16.75M_\odot)$ in the SMR scenario, or $(30M_\odot, 24M_\odot)$ in the RMR scenario. Throughout the paper, we use a single prime to identify the initially more massive stellar progenitor or "primary", and a double prime to denote the initially less massive progenitor or "secondary". This choice of initial masses also fixes the total mass of our BH binaries to $M = 13.5M_\odot$, quite close to the expected peak of the distribution for the total mass [12]. The mass of the stars is somewhat smaller than expected for the progenitors of BHs of these masses because we have neglected stellar winds, that lead to considerable mass loss prior to BH formation. Table I provides numerical values for the masses and radii of both the primary and secondary throughout the evolution in both the SMR and RMR scenarios. Appendix A 1 shows how this choice of initial masses leads to BHs of the desired final masses.

	SMR	RMR		SMR	RMR
$M'_{\rm Si}$	$35M_\odot$	$30M_\odot$	$R'_{\rm Si}$	$9.57R_\odot$	$8.78R_\odot$
$M''_{\rm Si}$	$16.75M_\odot$	$24M_\odot$	$R''_{\rm Si}$	$6.36R_\odot$	$7.76R_\odot$
$M''_{\rm Sf}$	$30M_\odot$	$35M_\odot$	$R''_{\rm Sf}$	$8.78R_\odot$	$9.57R_\odot$
$M'_{\rm C}$	$8.5M_\odot$	$8M_\odot$	$R'_{\rm C}$	$0.26R_\odot$	$0.26R_\odot$
$M''_{\rm C}$	$8M_\odot$	$8.5M_\odot$	$R''_{\rm C}$	$0.27R_\odot$	$0.27R_\odot$
$M'_{\rm BH}$	$7.5M_\odot$	$6M_\odot$	$R'_{\rm G}$	$3608R_\odot$	$3500R_\odot$
$M''_{\rm BH}$	$6M_\odot$	$7.5M_\odot$	$R''_{\rm G}$	$3500R_\odot$	$3608R_\odot$
$a_{\rm min}$	$17.9R_\odot$	$18.8R_\odot$	$a_{\rm noCE}$	$6981R_\odot$	$6758R_\odot$
$a_{\rm max}$	$8128R_\odot$	$8787R_\odot$	$a_{\rm mCE}$	$0.69R_\odot$	$0.63R_\odot$

TABLE I. Masses and length scales at various stages of the binary evolution in our SMR and RMR scenarios, as shown in Fig. 3. The only independent parameters are the main-sequence masses $M'_{\rm Si}$ and $M''_{\rm Si}$, which have been tuned to study final BH binaries with mass ratio $q = 0.8$. The other values are defined in the main text, and they are obtained using the analytical prescriptions presented in Appendix A.

The initial main-sequence stage of the evolution is shown as phase **a** in Fig. 3. Binaries are assumed to form on circular[3] orbits with initial semimajor axes a_0 drawn from the distribution described in Appendix A 2. We assume that the spins of the primary $\mathbf{S}'$ and secondary $\mathbf{S}''$ are initially aligned[4] with the orbital angular momentum $\mathbf{L}$. As the primary evolves, its envelope expands until it fills its Roche lobe, initiating stable mass transfer to the secondary (phase **b** in Fig. 3). The efficiency of mass transfer is usually parametrized via a parameter $f_a \in [0, 1]$: cf. Eq. (A9) of Appendix A 3. We assume this mass transfer continues until the primary has depleted its hydrogen envelope, leaving behind a helium core of mass $M'_C = 8.5M_\odot$ ($M'_C = 8M_\odot$) in the SMR (RMR) scenario. Following [12], we assume semiconservative mass transfer: the secondary accretes a fraction $f_a = 1/2$ of the mass lost by the primary, growing to a mass $M''_{Sf} = 30M_\odot$ ($M''_{Sf} = 35M_\odot$) in the SMR (RMR) scenario at the end of the mass-transfer episode. In principle mass transfer should also change the orbital separation, but we neglect this change as it is smaller than the width of the distribution of initial separations, as well as subsequent changes in the separation during the CE phase.

Following the end of mass transfer, the primary explodes in a SN (phase **c** in Fig. 3) producing a BH of mass $M'_{BH} = 7.5\ M_\odot$ ($M'_{BH} = 6\ M_\odot$) in the SMR (RMR) scenario. For simplicity, in our simulations the spin of this newly born BH is assumed to be maximal ($\chi_i = 1$, $i = 1\,, 2$) and aligned with its stellar progenitor. The SN ejecta are generally emitted asymmetrically, imparting a recoil velocity to the BH which is generally a fraction of the typical recoil velocities for protoneutron stars: $v_{\rm BH} \simeq (1 - f_{\rm fb})v_{\rm pNS}$, where $f_{\rm fb} \in [0, 1]$ is a "fallback parameter" (cf. Appendix A 4). This recoil tilts the orbital plane by an angle γ_1, and changes the semimajor axis and eccentricity to a_1 and e_1, respectively. These orbital changes depend on both the kick and the mass lost during the SN, as described in Appendix A 5.

After the SN explosion of the primary, the secondary evolves and expands. The primary raises tides on the swollen secondary, and dissipation may allow these tides to both circularize the orbit (so that the final eccentricity is $e_t \simeq 0$) and align the spin $\mathbf{S}''$ of the secondary with the orbital angular momentum $\mathbf{L}$, as shown in phase **d** of Fig. 3. This tidal alignment is described in much greater detail in Appendix A 6. Given the uncertainty in the efficiency of tidal alignment, we explore both extreme possibilities: complete circularization and alignment of $\mathbf{S}''$ ("Tides" in Fig. 2) and no circularization and alignment at all ("No Tides" in Fig. 2). As the secondary expands further, it fills its Roche lobe initiating a second phase

[3] The initial eccentricity has minimal effect. In fact we have repeated our calculations using an initially thermal distribution of eccentricities of the form $f(e) = 2e$, and we observed no significant difference in the final distribution of $\Delta\Phi$ and θ_{12}.

[4] The alignment of stellar spins in eclipsing binaries can be measured through the Rossiter-McLaughlin effect [34, 35]. Although many systems have aligned spins [36–38], there are notable exceptions [39]. We expect efficient tidal alignment in the progenitors of merging BH binaries, due to their small initial separations.

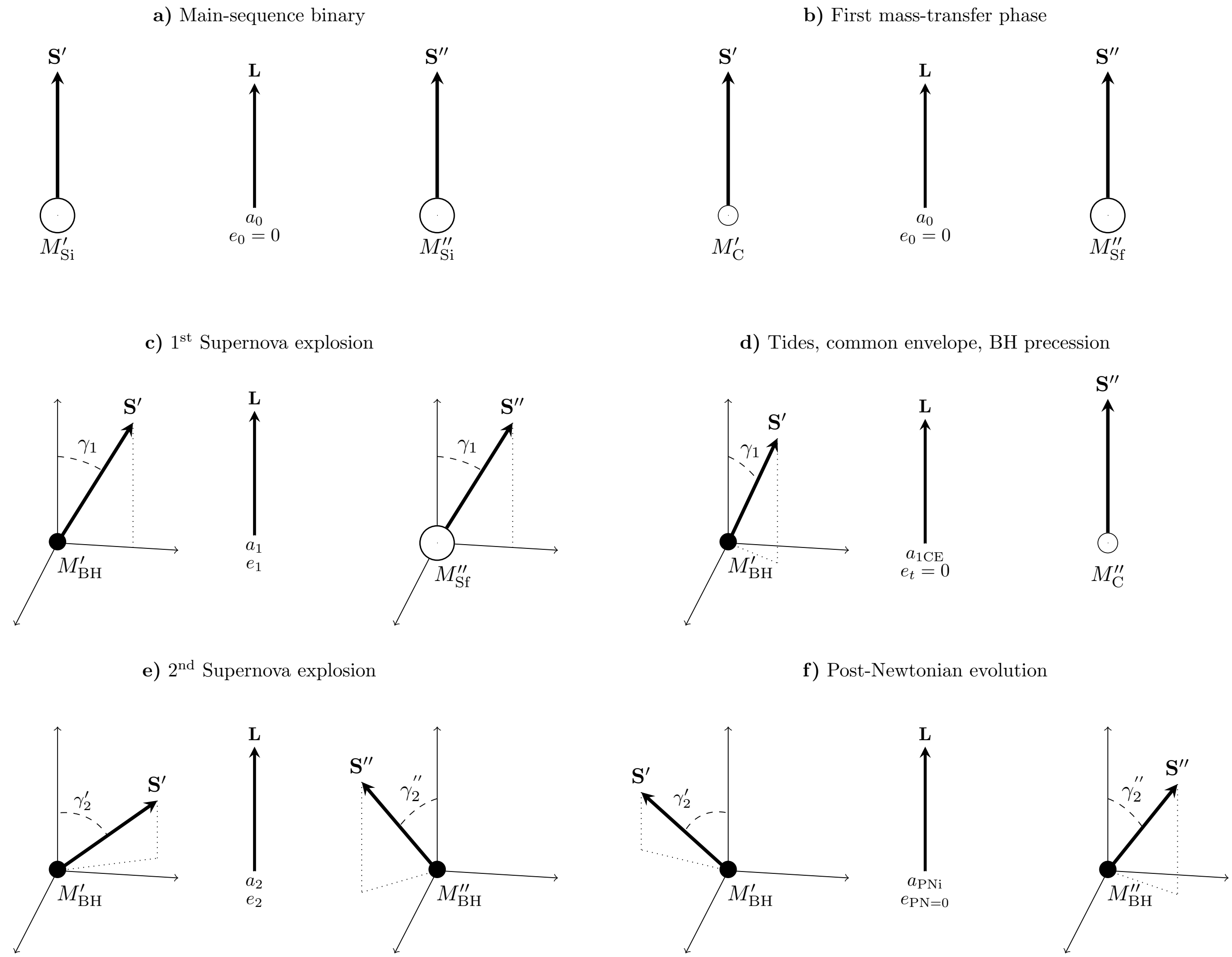

FIG. 3. A schematic representation of our model for BH binary formation and spin evolution. Empty circles represent stars, filled circles represent BHs. Phase (**a**) shows the initial main-sequence stellar binary. Mass transfer from the primary to the secondary (**b**) leads to a possible mass-ratio reversal. The first SN kick tilts the angle between the spins and the orbital plane (**c**). Tidal interactions can realign the stellar member of the binary (**d**). The second SN kick tilts the orbital plane again (**e**). Gravitational radiation shrinks and circularizes the binary before our explicit PN evolution begins (**f**).

of mass transfer. However, unlike the first mass-transfer event, this second mass-transfer phase will be highly unstable [40–42]. Instead of being accreted by the primary, most of this gas will expand into a CE about both members of the binary. Energy will be transferred from the binary's orbit to the CE, ultimately unbinding it from the system. This energy loss shrinks the semimajor axis of the binary from a_1 to $a_{\rm 1CE}$, as shown in phase **d** of Fig. 3. More details about CE evolution, including the relationship between a_1 and $a_{\rm 1CE}$, are provided in Appendix A 7. After the secondary loses its hydrogen envelope, the remaining helium core has a mass $M''_C = 8M_\odot$ ($M''_C = 8.5M_\odot$) in the SMR (RMR) scenario, as listed in Table I.

After the end of CE evolution, the naked helium core of the secondary rapidly completes its stellar evolution and explodes as a SN, as shown in phase **e** of Fig. 3. This explosion produces a BH of mass $M''_{\rm BH} = 6M_\odot$ ($M''_{\rm BH} = 7.5M_\odot$) in the SMR (RMR) scenario, as listed in Table I. We assume that this BH has a maximal spin that is aligned with the spin $\mathbf{S}''$ of its stellar progenitor, as we did for the primary. The SN leads to mass loss and a hydrodynamical recoil that change the semimajor axis and eccentricity of the binary to a_2 and e_2, respectively. It also tilts the orbital plane by an angle Θ that can be calculated using the same procedure as given for the first SN in Appendix A 5. The tilt resulting from the second SN is generally much smaller than that from the first SN ($\Theta \ll \gamma_1$) due to the comparatively larger orbital velocity following CE evolution. This tilt changes the angles between $\mathbf{L}$ and the spins $\mathbf{S}'$ and $\mathbf{S}''$ to γ'_2 and γ''_2, respectively. If tides efficiently align $\mathbf{S}''$ with $\mathbf{L}$ prior to the second SN, these angles are given by

$$\cos\gamma_2' = \cos\gamma_1\cos\Theta + \cos\varphi'\sin\gamma_1\sin\Theta\,, \tag{7}$$
$$\cos\gamma_2'' = \cos\Theta\ , \quad \text{(tides)} \tag{8}$$

where φ' is the angle between the projection of $\mathbf{S}'$ in the orbital plane before the SN and the projection of the change in $\mathbf{L}$ into this same initial orbital plane. If φ' is uniformly distributed (the direction of the SN kick of the secondary is uncorrelated with the spin of the primary), the second term on the right-hand side of Eq. (7) averages to zero, implying that $\gamma_2' > \gamma_2''$ for most binaries[5]. This is the mechanism for creating a binary BH population preferentially attracted to the $\Delta\Phi = \pm 180°$ family of spin-orbit resonances in the SMR scenario and the $\Delta\Phi = 0°$ family of resonances in the RMR scenario, as shown in Fig. 2.

If tides are inefficient, γ_2'' is instead given by

$$\cos\gamma_2'' = \cos\xi \qquad \text{(no tides)} \tag{9}$$
$$= \cos\gamma_1\cos\Theta - \sin\varpi\sin\gamma_1\sin\Theta\,, \tag{10}$$

where ξ is given by Eq. (A21), and ϖ is the angle between the projection of $\mathbf{S}''$ into the orbital plane before the second SN and the separation vector between the members of the binary. If ϖ is independent of φ' and uniformly distributed[6], the second term on the right-hand side of Eq. (10) also averages to zero, implying that $\gamma_2' \simeq \gamma_2''$. The small scatter about this relation follows from the lesser influence of the second SN kick ($\Theta \ll \gamma_1$), which implies that the identical first terms on the right-hand sides of Eqs. (7) and (10) dominate over the differing second terms. This explains the lack of preference for either family of resonances in the "No Tides" scenario shown in Fig. 2.

After the second SN, the BH binary is left in a non-relativistic orbit that gradually decays through the emission of gravitational radiation, as shown in phase **f** of Fig. 3. We calculate how this orbital decay reduces the semimajor axis and eccentricity using the standard quadrupole formula [32, 43]:

$$\frac{dt}{da} = -\frac{5}{64}\frac{c^5 a^3}{G^3 M^3}\frac{(1+q)^2}{q}(1-e^2)^{7/2}\left(1+\frac{73}{24}e^2+\frac{37}{96}e^4\right)^{-1}, \tag{11}$$

$$\frac{de}{da} = \frac{19}{12}\frac{e}{a}(1-e^2)\left(1+\frac{121}{304}e^2\right)\left(1+\frac{73}{24}e^2+\frac{37}{96}e^4\right)^{-1}. \tag{12}$$

To an excellent approximation, the BH spins simply precess about $\mathbf{L}$ during this stage of the evolution, leaving γ_2' and γ_2'' fixed to their values after the second SN. Once the semimajor axis reaches a value $a_{\rm PNi} = 1000M$ (in units where $G = c = 1$), we integrate higher-order PN equations of motion as described in Section III to carefully model how the orbit and spins evolve. We assume that radiation reaction circularizes the orbit ($e_{\rm PN} = 0$) by the time we start integrating the higher-order PN equations describing the precessional dynamics of the BH binary. This assumption is fully justified, as we will show by explicit integration in Section III B below.

C. Synthetic black-hole binary populations

In the previous Section, we presented fiducial scenarios for the formation of BH binaries characterized by three choices:

i) stable mass transfer prior to the first SN can preserve (SMR) or reverse (RMR) the mass ratio of the binary;

ii) hydrodynamic kicks generated by the SN can have a polar ($\theta_b = 10°$) or isotropic ($\theta_b = 90°$) distribution with respect to the exploding star's spin;

iii) tides do or do not circularize the orbit and align the spin $\mathbf{S}''$ of the secondary with the orbital angular momentum $\mathbf{L}$ prior to the second SN.

In this Section, we construct synthetic populations of BH binaries for the 8 different scenarios determined by the three binary choices listed above. To generate members of these synthetic populations, we perform Monte Carlo simulations[7] in which random values determine

i) the initial semimajor axis a_0 (Appendix A 2),

ii) the magnitude and direction of the kick produced in the first SN (Appendix A 4),

iii) the magnitude and direction of the kick produced in the second SN (Appendix A 4),

[5] Well separated distributions of γ_2' and γ_2'' require SN kick velocities that are comparable to the orbital velocity prior to the first SN, but much smaller than the orbital velocity before the second SN. Fortunately such kick velocities are well motivated, as described in Appendix A 4.

[6] This assumption is well justified because the primary and secondary spins precess at different rates [Ω_1 and Ω_2 given by Eqs. (14) and (15) below] and the precession timescale $t_{\rm pre} \sim \Omega_i^{-1}$ is short compared to the time $t_{\rm SN} \sim 10^6$ yrs between SN events. At lowest PN order, $t_{\rm pre} \sim t_{\rm LC}(v/c)^{-5}$, where $t_{LC} = GM/c^3 \simeq 5\times10^{-5}(M/10M_\odot)$ s is the light-crossing time. At a separation a we have $v/c \sim 5\times10^{-3}(M/10M_\odot)^{1/2}(a/R_\odot)^{-1/2}$, so $t_{\rm pre} \sim 0.5$ yr $\ll t_{\rm SN}$.

[7] We generated 10^8 binary progenitors to calculate the rates listed in Table II, which are therefore accurate to within $\sim 0.01\%$. To avoid cluttering, we only show a subsample of 10^4 progenitors in the figures of this Section.

Kicks	Tides	Mass transfer	$\nu_{\rm SN1}(\%)$	$\nu_{\rm mCE}(\%)$	$\nu_{\rm SN2}(\%)$	$\nu_{\rm H}(\%)$	$\nu_{\rm BH}(\%)$
Isotropic	On	SMR	32.50 (80.50)	26.53 (12.24)	2.66 (0.51)	0.04 (0.00)	38.27 (6.74)
Isotropic	On	RMR	32.55 (80.28)	34.86 (14.91)	2.97 (0.30)	0.04 (0.00)	29.59 (4.50)
Isotropic	Off	SMR	32.50 (80.50)	26.53 (12.24)	2.93 (0.60)	0.04 (0.01)	38.01 (6.65)
Isotropic	Off	RMR	32.55 (80.28)	34.86 (14.91)	3.01 (0.35)	0.04 (0.00)	29.54 (4.46)
Polar	On	SMR	31.84 (83.14)	26.68 (9.40)	3.29 (0.24)	0.01 (0.01)	38.18 (7.21)
Polar	On	RMR	31.86 (82.97)	34.88 (12.10)	3.65 (0.24)	0.02 (0.00)	29.58 (4.70)
Polar	Off	SMR	31.81 (83.16)	26.65 (9.38)	3.35 (0.52)	0.03 (0.01)	38.15 (6.93)
Polar	Off	RMR	31.84 (82.98)	34.89 (12.09)	3.65 (0.33)	0.04 (0.00)	29.59 (4.60)

TABLE II. Fraction of binaries ν (in percentage) that satisfy the following conditions, each of which successively *prevent* the formation of a merging BH binary: i) are unbound by the first SN ($\nu_{\rm SN1}$), ii) merge during the CE phase ($\nu_{\rm mCE}$), iii) are unbound by the second SN ($\nu_{\rm SN2}$), iv) do not merge within a Hubble time due to gravitational-radiation reaction ($\nu_{\rm H}$). The final column is the fraction $\nu_{\rm BH} = 1-(\nu_{\rm SN1}+\nu_{\rm mCE}+\nu_{\rm SN2}+\nu_{\rm H})$ of all simulated binaries that form merging BH binaries. In parentheses we list the corresponding fractions if SN kicks are not suppressed by fallback (i.e. if we set $f_{\rm fb}=0$ rather than $f_{\rm fb}=0.8$): see Appendix A 4).

iv) the angles φ' and ϖ specifying the directions of the spins $\mathbf{S}'$ and $\mathbf{S}''$ before the second SN (Section II B),

v) the angle $\Delta\Phi$ between the projections of the BH spins in the orbital plane at separation $a_{\rm PNi}$.

The angles φ', ϖ, and $\Delta\Phi$ in items iv) and v) above are uniformly distributed in the range $[0, 2\pi]$. The synthetic populations generated in this procedure determine the initial conditions for the PN equations of motion described in Section III.

A binary-star system can *fail* to produce a merging BH binary for one of the following reasons:

i) it is unbound by the first SN ($e_1 > 1$);

ii) it merges during the CE evolution between the two SN ($a_{1CE} < a_{\rm mCE}$);

iii) it is unbound by the second SN ($e_2 > 1$);

iv) the time t required for gravitational radiation to shrink the semimajor axis from a_2 to $a_{\rm PNi}$, found by solving the coupled PN equations (11) and (12), exceeds the Hubble time $t_{\rm H} \simeq 10^{10}$ Gyr.

Table II lists the fraction of simulated binaries $\nu_{\rm SN1}$, $\nu_{\rm mCE}$, $\nu_{\rm SN2}$, and ν_H that fail to produce merging BH binaries for reasons i) through iv) listed above, as well as the fraction $\nu_{\rm BH} = 1-(\nu_{\rm SN1}+\nu_{\rm mCE}+\nu_{\rm SN2}+\nu_{\rm H})$ that *do* evolve into such binaries.

The failure fractions indicate the relative importance of different physical phenomena. To emphasize the sensitivity of our results to the highly uncertain SN kicks, we also show how these fractions change when the BH kick $v_{\rm BH} = (1-f_{\rm fb})v_{\rm pNS}$ fully equals that imparted to the protoneutron star ($f_{\rm fb}=0$) rather than our canonical choice ($f_{\rm fb}=0.8$); see Appendix A 4 for more details. Stronger kicks unbind more binaries during the first SN, increasing $\nu_{\rm SN1}$ and thereby reducing the overall fraction $\nu_{\rm BH}$ of binaries that survive to form BH binaries. This qualitatively agrees with results of detailed population-synthesis models; see models S, V8, and V9 in [44]. We adopt $f_{\rm fb}=0.8$ in the remainder of the paper.

Fig. 4 shows how the choices that define our fiducial scenarios affect whether SN kicks unbind the binaries. One result apparent from this plot (and supported by the failure fractions $\nu_{\rm SN}$ listed in Table II) is that the probability of unbinding the system depends only weakly on whether the SN kicks are isotropic or polar. This is consistent with the findings of [45], which suggest mild sensitivity to θ_b when the typical kick velocity $v_{\rm BH} \sim 50$ km/s is small compared to the orbital velocity $v_0 \simeq 2.4\times10^3(M/30M_\odot)^{1/2}(a/R_\odot)^{-1/2}$ km/s. Fig. 4 also shows the effect of tides on the fraction $\nu_{\rm BH}$ of BH binaries produced. In the absence of tidal dissipation ("No Tides"), the binaries have nonzero eccentricity ($e_i \neq 0$) when the second SN occurs. Eq. (A17) shows that the final semimajor axis a_f has additional dependence on the true anomaly ψ_i in this limit, broadening the distribution of a_f, as can be seen in the right panel of Fig. 4. The kicks can add coherently to the large orbital velocities near pericenter of highly eccentric orbits, allowing binaries to become unbound even after CE evolution has reduced the semimajor axis: cf. the handful of light-gray (green) points with $a_{1CE} \lesssim 10R_\odot$ in the right panel of Fig. 4). This increases the fraction $\nu_{\rm SN2}$ of binaries unbound in the second SN when tides are "Off" in Table II. The importance of CE evolution can be seen as well: virtually all binaries that fail to form a CE ($a_{1CE} \gtrsim 10^4 R_\odot$) are unbound by the second SN. Binaries bound tightly enough to survive the second SN almost always manage to merge through GW emission in less than a Hubble time ($\nu_{\rm H} \ll 1$).

III. POST-NEWTONIAN INSPIRAL

A. Post-Newtonian equations of motion

At large orbital separations, the dynamics of BH binaries in vacuum can be approximated by expanding the Einstein equations in a perturbative PN series, where the perturbative parameter is the ratio v/c of the orbital velocity to the speed of light. For historical reasons, one

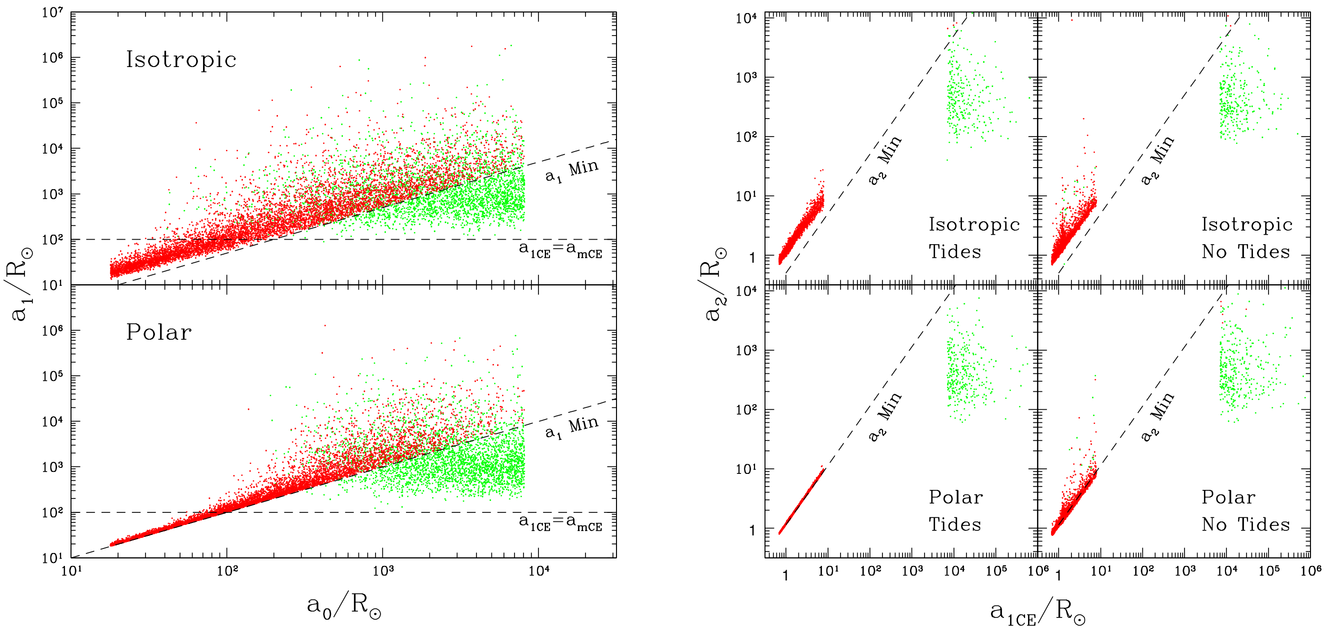

FIG. 4. (Color online.) Scatter plot showing the change in the semimajor axis due to the first (left panel: $a_0 \to a_1$) and second (right panel: $a_{1\mathrm{CE}} \to a_2$) SN. All plots refer to the SMR scenario, but the behavior in the RMR scenario is very similar. Darker (red) dots represent binaries that remain bound after each explosion, while lighter (green) dots correspond to binaries that are unbound. Dashed lines show the minimum post-SN semimajor axis $a_{f,\mathrm{Min}}$ given by Eq. (A23) and the critical semimajor axis a_{mCE} given by Eq. (A34) below which binaries merge during CE evolution. Kicks are too small to saturate the isotropic limit $a_{f,\mathrm{Min}}$ for $a_i \lesssim 10^2 R_\odot$.

usually says that a quantity is expanded up to kPN order if all terms up to order $(v/c)^{2k}$ are retained. Following common practice in the general relativity literature, in this Section we will use geometrical units such that $G = c = 1$.

The PN approximation can describe the evolution of stellar-mass binaries down to separations $a \sim 10M$ (i.e. $a \sim 10^{-4} R_\odot$ for a BH binary with $M = 10M_\odot$), beyond which fully nonlinear numerical simulations are needed [46–49]. GW detection templates depend on the binary parameters when the system enters the sensitivity band of the detectors, which is well into the regime where PN corrections are significant, but astrophysical models of BH evolution (as implemented e.g. in population-synthesis codes) have so far neglected all general-relativistic effects. The main goal of this Section is to show that solving the PN equations of motion is necessary to determine the orientation of BH spins when binaries enter the sensitivity band of GW detectors such as Advanced LIGO/Virgo and the Einstein Telescope.

The PN equations of motion and gravitational waveforms for spinning BH binaries were derived by several authors (see e.g. [50–52]). Our previous investigations of spin dynamics considered binaries on circular orbits; as shown in Section III B below, this is an excellent approximation for most binaries in our sample. They also included high-order PN terms such as the monopole-quadrupole interaction and the spin-spin self interactions [9–11], that we report for completeness below.

For circular orbits with radius a and orbital velocity $v = (GM/a)^{1/2}$, the "intrinsic" dynamics of a binary system depends on 10 variables: the two masses (m_1, m_2), the spins $\mathbf{S}_1$ and $\mathbf{S}_2$ and the direction of the orbital angular momentum $\hat{\mathbf{L}}$. At the PN order we consider both spin magnitudes and the mass ratio q remain fixed during the inspiral. This leaves 7 independent degrees of freedom. Because BHs are vacuum solutions of the Einstein equations, there is only one physical scale in the problem (the total mass of the binary M). Rescaling all quantities relative to the mass M, we are left with 6 "intrinsic" parameters.

It is convenient to analyze the precessional dynamics in the frame where the direction of the orbital momentum $\hat{\mathbf{L}}$ lies along the z-axis. If we take (say) the x-axis to be oriented along the projection of $\mathbf{S_1}$ on the orbital plane (see Fig. 1 in [6]), we are effectively imposing 3 additional constraints just by our choice of the reference frame (2 components of $\hat{\mathbf{L}}$ and 1 component of $\mathbf{S_1}$ are set equal to zero). Then the only 3 variables describing precessional dynamics are the angles θ_1, θ_2 and $\Delta\Phi$, as defined in Eqs. (2) and (3). The angle between the two spins θ_{12} is related to the other independent variables as follows:

$$\cos\theta_{12} = \sin\theta_1 \sin\theta_2 \cos\Delta\Phi + \cos\theta_1 \cos\theta_2 . \qquad (13)$$

In summary, for any given binary with intrinsic parameters (q, χ_1, χ_2), the precessional dynamics is encoded in the variables $(\theta_1, \theta_2, \Delta\Phi)$ as functions of the orbital velocity v or (equivalently) of the orbital frequency $\omega = v^3/M$. These variables can be evolved forward in time by integrating the following PN equations of motion:

$$\frac{d\mathbf{S_1}}{dt} = \mathbf{\Omega_1} \times \mathbf{S_1}, \qquad M\mathbf{\Omega_1} = \eta v^5 \left(2 + \frac{3q}{2}\right) \hat{\mathbf{L}} + \frac{v^6}{2M^2} \left[\mathbf{S_2} - 3\left(\hat{\mathbf{L}} \cdot \mathbf{S_2}\right) \hat{\mathbf{L}} - 3q\left(\hat{\mathbf{L}} \cdot \mathbf{S_1}\right) \hat{\mathbf{L}}\right]; \tag{14}$$

$$\frac{d\mathbf{S_2}}{dt} = \mathbf{\Omega_2} \times \mathbf{S_2}, \qquad M\mathbf{\Omega_2} = \eta v^5 \left(2 + \frac{3}{2q}\right) \hat{\mathbf{L}} + \frac{v^6}{2M^2} \left[\mathbf{S_1} - 3\left(\hat{\mathbf{L}} \cdot \mathbf{S_1}\right) \hat{\mathbf{L}} - \frac{3}{q}\left(\hat{\mathbf{L}} \cdot \mathbf{S_2}\right) \hat{\mathbf{L}}\right]; \tag{15}$$

$$\frac{d\hat{\mathbf{L}}}{dt} = -\frac{v}{\eta M^2} \frac{d}{dt}(\mathbf{S_1} + \mathbf{S_2}); \tag{16}$$

$$\begin{aligned}\frac{dv}{dt} = \frac{32}{5} \frac{\eta}{M} v^9 \Bigg\{ & 1 - v^2 \frac{743 + 924\eta}{336} + v^3 \left[4\pi - \sum_{i=1,2} \chi_i (\hat{\mathbf{S}}_\mathbf{i} \cdot \hat{\mathbf{L}}) \left(\frac{113}{12} \frac{m_i^2}{M^2} + \frac{25}{4}\eta\right)\right] \\
& + v^4 \left[\frac{34103}{18144} + \frac{13661}{2016}\eta + \frac{59}{18}\eta^2 + \frac{\eta\chi_1\chi_2}{48} \left(721(\hat{\mathbf{S}}_\mathbf{1} \cdot \hat{\mathbf{L}})(\hat{\mathbf{S}}_\mathbf{2} \cdot \hat{\mathbf{L}}) - 247(\hat{\mathbf{S}}_\mathbf{1} \cdot \hat{\mathbf{S}}_\mathbf{2})\right)\right. \\
& \left. + \frac{1}{96} \sum_{i=1,2} \left(\frac{m_i\chi_i}{M}\right)^2 \left(719(\hat{\mathbf{S}}_\mathbf{i} \cdot \hat{\mathbf{L}})^2 - 233\right)\right] - v^5 \pi \frac{4159 + 15876\eta}{672} \\
& + v^6 \left[\frac{16447322263}{139708800} + \frac{16}{3}\pi^2 - \frac{1712}{105}(\gamma_E + \ln 4v) + \left(\frac{451}{48}\pi^2 - \frac{56198689}{217728}\right)\eta + \frac{541}{896}\eta^2 - \frac{5605}{2592}\eta^3\right] \\
& + v^7 \pi \left[-\frac{4415}{4032} + \frac{358675}{6048}\eta + \frac{91495}{1512}\eta^2\right] + O(v^8) \Bigg\};\end{aligned} \tag{17}$$

where $\eta = m_1 m_2/M^2$ and $\gamma_E \simeq 0.577$ is Euler's constant.

The leading terms in Eqs. (14)-(15), up to $\mathcal{O}(v^5)$ or 2.5PN order, describe precessional motion about the direction of the orbital angular momentum $\hat{\mathbf{L}}$. We assumed that these terms dominated during the PN inspiral of the previous Section, allowing γ_2' and γ_2'' to remain fixed at $a > 1000M$. Spin-orbit couplings appear at 3PN, and they are the reason for the existence of the resonant configurations [6]. From Eq. (16) we see that the direction of the angular momentum evolves on a precessional timescale, while Eq. (17) implies that its magnitude decreases on the (longer) radiation-reaction timescale due to GW emission. The leading (quadrupolar) order of Eq. (17) is equivalent to the circular limit of Eq. (11) when we recall that $v^2 = M/a$.

Higher-order PN terms in the equations of motion were recently computed [53]. We modified Eqs. (14)-(17) to include these new terms, finding that they affect the late-time dynamics of individual binaries but have negligible influence on the statistical behavior of our samples. The robustness of these statistical properties under the inclusion of higher-order PN terms was already noted in [9–11]. For completeness we retained the higher-order PN terms that will be reported in [53] in our Monte Carlo simulations, but we stress again that they have no observable impact on our results.

At a given separation a, Schnittman's resonant configurations can be found by forcing the three vectors $\mathbf{S}_1$, $\mathbf{S}_2$ and $\hat{\mathbf{L}}$ to lie in a plane ($\Delta\Phi = 0^\circ, \pm 180^\circ$) and by imposing the constraint that the second time derivative of $\cos\theta_{12}$ vanish [6]. A one-parameter family of configurations with $\Delta\Phi = 0^\circ$ and $\theta_1 < \theta_2$ satisfies this resonant constraint, as does a second one-parameter family with $\Delta\Phi = \pm 180^\circ$ and $\theta_1 > \theta_2$. As a decreases due to GW emission, the curves determined by these one-parameter families change, sweeping through a large region of the (θ_1, θ_2) parameter space. The resonant constraint evolves toward the diagonal $\theta_1 = \theta_2$ as $a \to 0$. Individual resonant binaries move towards the diagonal in the (θ_1, θ_2) plane along trajectories over which the projection $\mathbf{S_0} \cdot \hat{\mathbf{L}}$ of the spin combination $\mathbf{S_0}$ defined in the effective-one-body model [54],

$$\mathbf{S_0} = (1 + q)\mathbf{S_1} + (1 + q^{-1})\mathbf{S_2}, \tag{18}$$

is approximately constant (cf. Figs. 1 and 2 of [9]). Resonant configurations with $\Delta\Phi = 0$ tend to align the two spins with each other, so that $\theta_{12} \to 0^\circ$ near merger. On the other hand, configurations with $\Delta\Phi = \pm 180^\circ$ identified by their constant value of $\mathbf{S_0} \cdot \hat{\mathbf{L}}$ evolve towards

$$\cos\theta_{12} \to 2\left[\frac{(1+q)\mathbf{S_0}\cdot\hat{\mathbf{L}}}{(\chi_1+q\chi_2)M^2}\right]^2 - 1\ . \tag{19}$$

B. Initial conditions for the PN evolution

By construction, all of the merging BH binaries produced in Section II have $M = 13.5 M_\odot$, $q = 0.8$, and $\chi_1 = \chi_2 = 1$. For this mass ratio and these spin magnitudes, binaries become attracted towards resonances ("resonant locking") at separations $a \lesssim 100M$ [6]. Previous studies suggest that the spin-orbit resonances remain influential provided $q \gtrsim 0.4$ and $\chi_i \gtrsim 0.5$ [9–11]. To be safe, we begin following binaries at an initial separation $a_{\rm PNi} = 1000M$ large enough so that we can neglect spin-spin coupling at greater separations [9]. Recall that the mass ratio was defined such that $q \equiv m_2/m_1 \leq 1$. In the SMR scenario, the primary yields the larger BH ($M'_{\rm BH} > M''_{\rm BH}$), so the angles are initialized to be

$$\theta_1 = \gamma'_2, \qquad \theta_2 = \gamma''_2\ . \tag{20}$$

In the RMR case, the primary transfers so much mass to the secondary prior to the first SN that it actually produces the smaller BH ($M'_{\rm BH} < M''_{\rm BH}$), implying that we must reverse our initialization:

$$\theta_1 = \gamma''_2, \qquad \theta_2 = \gamma'_2\ . \tag{21}$$

Although our decision to neglect spin-spin coupling for $a > a_{\rm PNi}$ allows us to initialize θ_i in this manner, the lower-order spin-orbit coupling allows $\Delta\Phi$ to evolve on the precessional timescale, which is short compared to the time it takes to inspiral from a_2 to $a_{\rm PNi}$. We can therefore choose $\Delta\Phi$ at $a_{\rm PNi}$ to be uniformly distributed in the range $[-180^\circ, +180^\circ]$. Finally, since gravitational radiation is very efficient at circularizing the orbit [to leading order $e \propto a^{19/12}$; see Eq. (12)], we assume that all BH binaries have circularized by the time they reach $a_{\rm PNi}$. We checked this assumption by numerically integrating Eq. (12) from a_2 to $a_{\rm PNi}$ after initializing it with the values e_2 predicted following the second SN; the residual eccentricity at $a_{\rm PNi}$ was less than 10^{-4} for all BH binaries in our samples.

C. Results

We evolved 10^3 BH binaries for each of the 8 different fiducial astrophysical scenarios described in Section II C from an initial separation[8] $a_{\rm PNi} = 1000M$ to a final separation $a_{\rm PNf} = 10M$. This final separation roughly indicates where the PN approximation breaks down and full numerical relativity becomes necessary [46–49]. To reduce the Poisson noise in the histograms of Fig. 2, we used larger samples of 10^4 BH binaries. We integrated the PN equations (14)-(17) using a STEPPERDOPR5 integrator in C++ [55], progressively refining the time steps at small separations (see [9] for further details).

In Fig. 5, we show the evolution of the dynamical variables $(\theta_1, \theta_2, \Delta\Phi)$ for both the SMR and RMR scenarios with efficient tides and isotropic kicks. As already anticipated in the introduction, efficient tidal interactions lead to spin orientations that are strongly affected by spin-orbit resonances. When binaries are brought close enough to resonant configurations by precessional motion and gravitational-radiation reaction, they no longer precess freely through all values of $\Delta\Phi$, but instead oscillate about the resonant configurations [6, 9]. In the SMR scenario, the initial orientation of the spins is such that $\theta_1 > \theta_2$, and the binaries lock into resonances with $\Delta\Phi = \pm 180^\circ$ [darker (red) points in Fig. 5]. In contrast, in the RMR scenario the initial spins have $\theta_1 < \theta_2$ and the binaries lock into resonances with $\Delta\Phi = 0^\circ$ [lighter (green) points in Fig. 5]. Once the binaries are trapped near resonances, they evolve toward the diagonal in the (θ_1, θ_2) plane, as seen in the left panel of Fig. 5. This corresponds to $\theta_{12} \to 0^\circ$ for binaries near the $\Delta\Phi = 0^\circ$ family of resonances (RMR scenario). As seen in the right panel of Fig. 5, there is a much broader range of final values for θ_{12} in the SMR scenario, because these final values depend on the initial astrophysical distribution of $\mathbf{S_0} \cdot \hat{\mathbf{L}}$ according to Eq. (19).

Fig. 6 shows that spin-orbit resonances can have an even stronger effect on BH binaries when SN kicks are polar (aligned within $\theta_b = 10^\circ$ of the stellar spin [56]). As discussed in Appendix A 5, exactly polar kicks tilt the orbital plane by an angle Θ given by Eq. (A24), which can only attain a maximum value $\cos^{-1}(2\beta)^{-1/2}$ (where $\beta = M_f/M_i$ is the ratio of the total binary mass before and after the SN) without unbinding the binary. For $\beta \simeq 0.9$, as in our SMR and RMR scenarios, $\Theta \lesssim 40^\circ$, and kicks are rarely large enough even to saturate this limit. This explains the much narrower distribution of

[8] The $a = 1000M$ snapshots in the figures of this Section are taken shortly after the beginning of the PN evolution. The angle $\Delta\Phi$ varies on the precessional timescale and can therefore change quite rapidly before the separation decreases appreciably on the longer inspiral timescale. The initial clustering in $\Delta\Phi$ visible in the top-right panels of Figs. 5 and 6 is *not* a resonant effect, as the binaries continue to sweep through all values of $\Delta\Phi$ at these large separations. It results instead from the different rates at which binaries in the SMR and RMR populations precess, segregating the groups from each other during the first few precessional cycles. This behavior is better illustrated by the animations available online at the following URLs, which refer to efficient tides with isotropic kicks, efficient tides with polar kicks, inefficient tides with isotropic kicks, and inefficient tides with polar kicks, respectively:
`http://www.phy.olemiss.edu/~berti/tides_isotr.gif`
`http://www.phy.olemiss.edu/~berti/tides_polar.gif`
`http://www.phy.olemiss.edu/~berti/notides_isotr.gif`
`http://www.phy.olemiss.edu/~berti/notides_polar.gif`

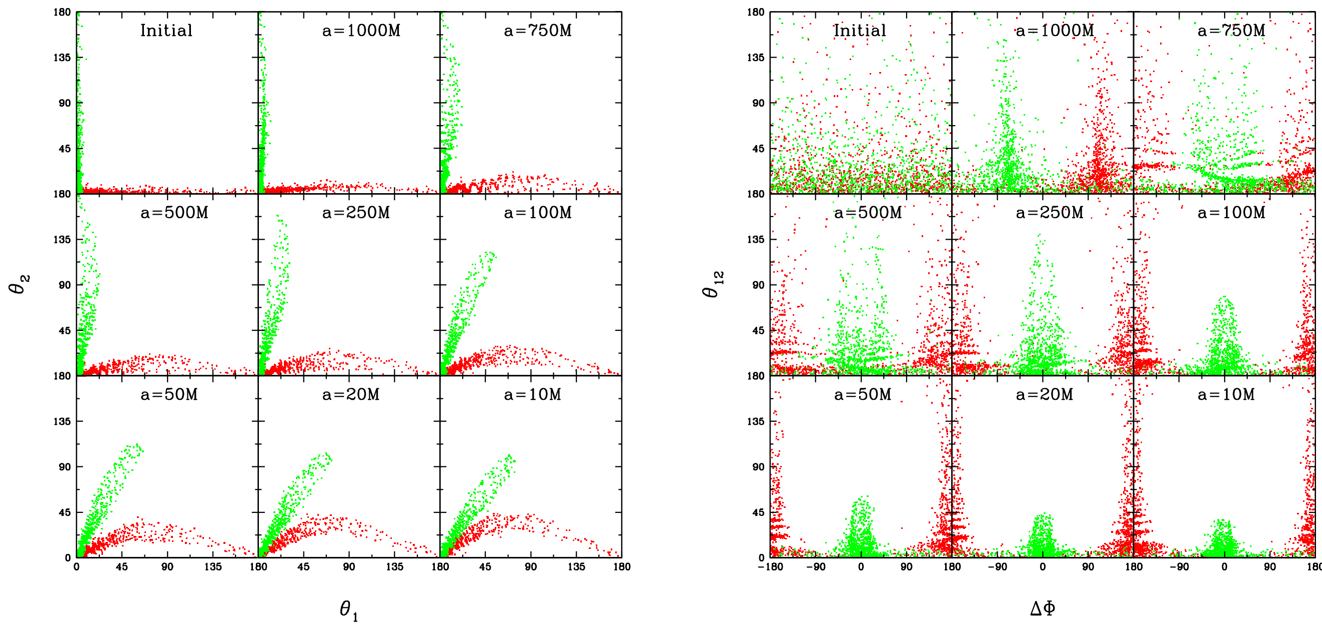

FIG. 5. (Color online.) Scatter plots of the PN inspiral of maximally spinning BH binaries with mass ratio $q = 0.8$ from an initial separation $a_{\rm PNi}$ just above $1000M$ to a final separation $a_{\rm PNf} = 10M$. The left panel shows this evolution in the (θ_1, θ_2) plane and the right panel shows the evolution in the $(\Delta\Phi, \theta_{12})$ plane. Darker (red) and lighter (green) dots refer to the SMR and RMR scenarios, respectively. The initial distribution for these Monte Carlo simulations was constructed from an astrophysical model with efficient tides and isotropic kicks. An animated version of this plot is available online at the URL: `http://www.phy.olemiss.edu/~berti/tides_isotr.gif`

initial values of θ_i in the left panel of Fig. 6 compared to Fig. 5. Binaries with these smaller initial misalignments are more easily captured into resonances, as can be seen from the near total segregation of the SMR and RMR populations in $\Delta\Phi$ by the time the binaries reach $a_{\rm PNf} = 10M$ in the right panel of Fig. 6.

In our model, two physical mechanisms are responsible for changing BH spin orientations: SN kicks and tidal alignment. Both mechanisms are critical: kicks generate misalignments between the spins and the orbital angular momentum, but only tides can introduce the asymmetry between these misalignments that causes one family of spin-orbit resonances (the $\Delta\Phi = \pm 180°$ family in the SMR scenario, the $\Delta\Phi = 0°$ family in the RMR scenario) to be favored over the other. When tidal effects are removed, as shown in Figs. 7 and 8, BH binaries are formed with $\theta_1 \simeq \theta_2$ on average. Being symmetric under exchange of the two BHs, the evolution in the SMR and RMR scenarios is almost identical. As expected, the binaries do not lock into resonant configurations, instead precessing freely during the whole inspiral. In the late stages of inspiral, the binaries tend to pile up at $\Delta\Phi = \pm 90°$, i.e. they spend more time in configurations where the projections of the two spins on the orbital plane are orthogonal to each other. Unlike the spin-orbit resonances, configurations with $\Delta\Phi = \pm 90°$ are not steady-state solutions to the spin-evolution equations in the absence of radiation reaction [6]. The pile up at these configurations however is an essential complement to the spin-orbit resonances for preserving the well known result that initially isotropic spin distributions remain isotropic (see e.g. [13]). The physical origin of this phenomenon merits further investigation.

IV. COMPARISON WITH POPULATION SYNTHESIS

We have demonstrated that viable astrophysical formation channels can result in BH binaries that are strongly affected by spin-orbit resonances during the late PN portion of the inspiral but before the binary enters the GW detection band. Therefore PN resonances can affect the observed dynamics of precessing binaries. Even more interestingly, the distribution of the angles $\Delta\Phi$ and θ_{12} is a diagnostic tool to constrain some of the main physical mechanisms responsible for BH binary formation (namely the efficiency of tides, and whether mass transfer can produce mass-ratio reversal).

However, some caveats are in order. Even our limited exploration of the parameter space of BH binary formation models has shown that the influence of PN resonances depends sensitively on highly uncertain factors, such as the magnitude and direction of SN kicks, or the mass ratio and semimajor axis of the binary at various stages of its evolution. In this Section, we argue that: (i)

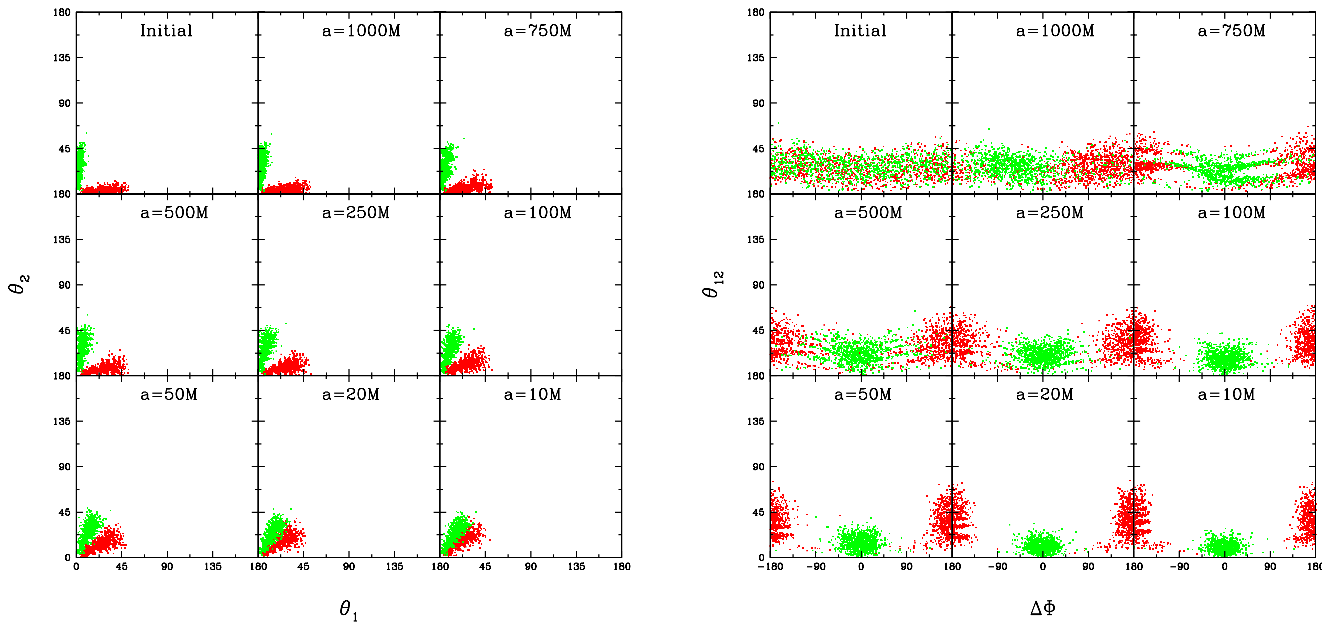

FIG. 6. (Color online.) Scatter plots of the same quantities shown in Fig. 5 for an astrophysical model with efficient tides and polar kicks. For an animated version of this plot, see: `http://www.phy.olemiss.edu/~berti/tides_polar.gif`

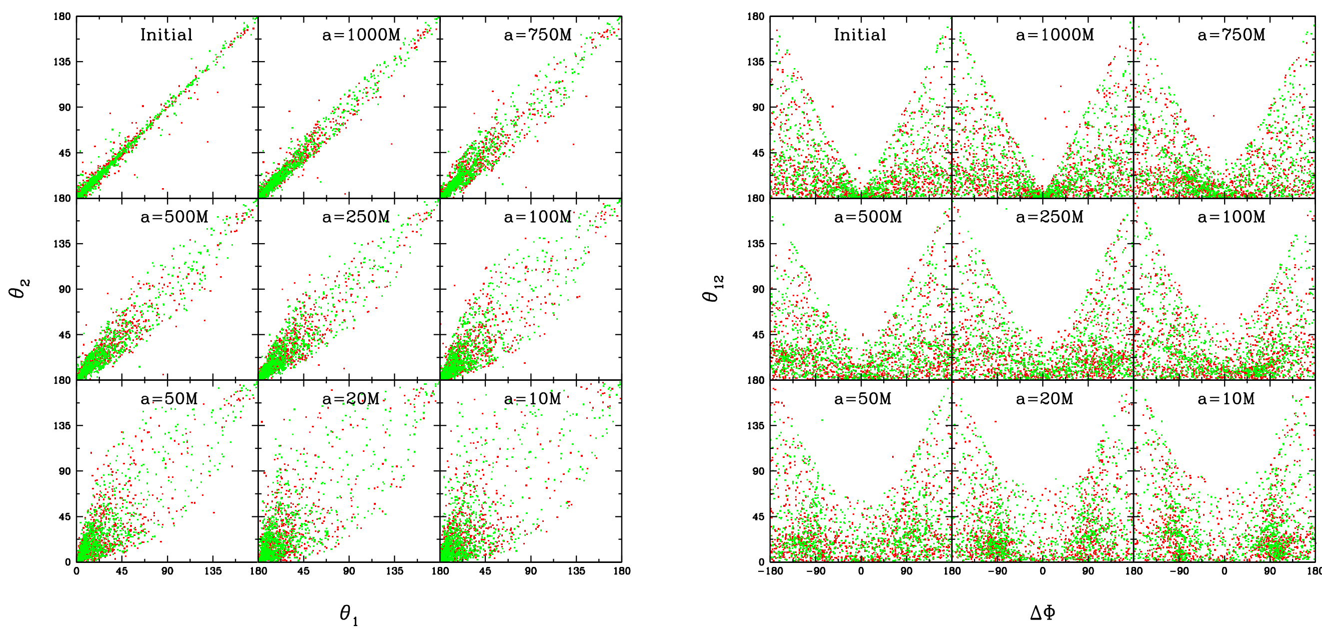

FIG. 7. Scatter plots of the same quantities shown in Fig. 5 for an astrophysical model with inefficient tides and isotropic kicks. For an animated version of this plot, see: `http://www.phy.olemiss.edu/~berti/notides_isotr.gif`

our fiducial scenarios are indeed representative of the predictions of more sophisticated population-synthesis models (Section IV A); and (ii) as a consequence, observations of spin-orbit resonances through their GW signatures can provide valuable insight into BH binary formation channels (Section IV B).

A. Is our fiducial scenario representative?

In our study we chose to follow the evolution of two binary progenitors in detail, using a specific formation channel. The resulting BH binaries resemble at least qualitatively the low-mass BH binaries that can be

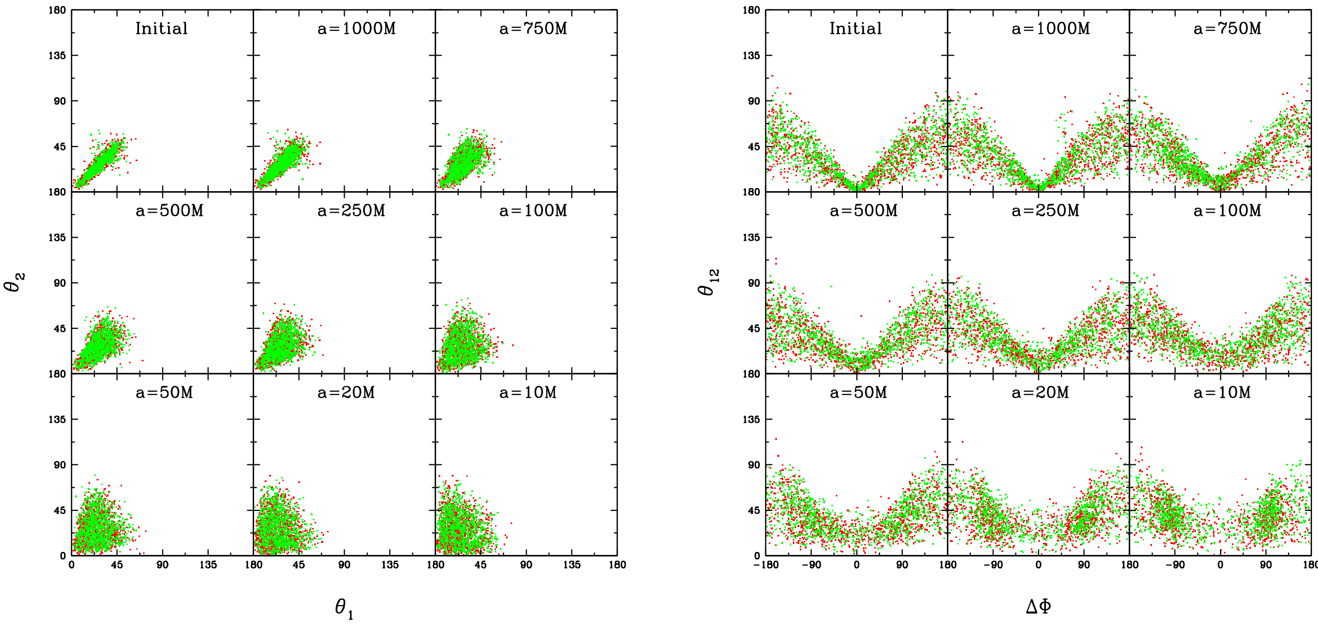

FIG. 8. Scatter plots of the same quantities shown in Fig. 5 for an astrophysical model with inefficient tides and polar kicks. For an animated version of this plot, see: `http://www.phy.olemiss.edu/~berti/notides_polar.gif`

formed through a wide range of compact-object formation scenarios at a range of metallicities: see e.g. [12].

An important assumption made in this study is that of negligible mass loss. Current calculations suggest that the progenitors of the most commonly detected BH binaries will in fact have low metallicity and strongly suppressed mass loss [12]. The advantage of our approach is that by neglecting mass loss and focusing on a pair of fiducial binaries we can perform a "controlled experiment" to highlight how different physical phenomena influence the efficiency of PN resonance locking. Variations in the range of initial binary masses, wind mass loss and other mass transfer modes will affect the mass distribution of the binaries and the initial distribution of the misalignment angles (θ_1, θ_2), but not our main qualitative predictions, that should be rather robust.

This study included what we believe to be the most important physical mechanisms that could trap binaries in resonant configurations, but it is certainly possible that additional ingredients overlooked in our model could complicate our simple interpretation of the results. For example, our argument relies on a universal and deterministic relationship between stellar masses and compact remnants. By contrast, some studies suggest that the relationship between the initial and final mass may depend sensitively on interior structure [57], rotation, or conceivably even stochastically on the specific turbulent realization just prior to explosion. As a concrete example, recent simulations of solar-metallicity SN explosions by Ugliano et al. [57] (including fallback) and O'Connor and Ott [58] (neglecting fallback) have produced non-monotonic relationships between the progenitor and final BH masses. Likewise, our argument makes the sensible assumption that BH spins are aligned with the spin of their stellar progenitor, but neutron star observations suggest that the protoneutron star's spin axis may be perturbed in a SN [59].

Our case studies of binary evolution omit by construction many of the complexities present in more fully developed population-synthesis models. The inclusion of additional physics presents interesting opportunities for a more detailed understanding of the connection between poorly constrained assumptions in population-synthesis models and GW observations. Some of the limitations we imposed on our model – and therefore, interesting opportunities for follow-up studies – are listed below: (1) we follow the formation and evolution of only two progenitor binaries, rather than monitoring a distribution of masses; (2) we only consider maximally spinning BHs, while we should consider astrophysically motivated spin magnitude distributions; (3) we adopt very simple prescriptions for mass transfer and evolution, which have minimal feedback onto the structure and evolution of each star; (4) we employ an extreme "all or nothing" limit for tidal interactions; (5) we assume that BHs are kicked with a specific fraction of the overall SN kick strength; (6) we neglect stellar mass loss, magnetic braking and other phenomena that can occur in different formation scenarios.

In summary: while our fiducial scenario provides a representative environment to explore the physics of PN resonances, the specific mass distribution and the quantitative distribution of the misalignment angles at the beginning of the PN-driven inspiral will depend on detailed binary-evolution physics which is neglected by construction in our toy model. It will be interesting to initialize our Monte Carlo simulations using more comprehensive binary-evolution models that include a distribution of progenitor masses, track tidal backreaction on the spins and orbit, and model in more detail mass transfer and the modifications it introduces to core and stellar evolution.

B. Observational payoff

Let us provide a specific example to illustrate these uncertainties and their potential observational payoff. Our fiducial model assumed relatively low-mass BHs. These systems receive strong SN kicks (due to small fallback) and are more significantly influenced by CE contraction (because of the greater relative effect of the envelope binding energy). By contrast, more massive BHs in the `StarTrack` sample will accrete a significantly higher fraction of their pre-SN mass, which drastically suppresses the typical kick magnitude. As a result, massive BH binaries can be expected to have BH spins more aligned with the orbital angular momentum.

This sort of qualitative difference between low- and high-mass BH binaries presents an opportunity for GW detectors. The most easily measurable quantity in GW observations is the "chirp mass" $M_{\rm chirp} = \eta^{3/5} M$, where $M = m_1 + m_2$ is the total binary mass and $\eta = m_1 m_2/M^2$ is the symmetric mass ratio (see e.g. [60, 61]). Therefore, even though current simulations suggest that the detected sample will be dominated by high-mass, nearly aligned BH binaries, observations can clearly identify the low-mass sample, which should exhibit significant initial misalignment and more interesting precessional dynamics. Given the significant uncertainties in population-synthesis models, even upper limits on the spin-orbit misalignment for high-mass BH binaries would be extremely valuable, either to corroborate the expectation of strong alignment or to demonstrate the significance of SN kicks for high-mass BHs.

Based on our prototype study, let us assume that each PN resonance is an unambiguous indicator of a specific fomation scenario: hypothetical GW measurements of angles $\Delta\Phi \sim \pm 180°$ mean efficient tides in the "standard mass ratio" (SMR) scenario; measurements of $\Delta\Phi \sim 0°$ mean that mass reversal also occurred (RMR); finally, $\Delta\Phi \sim \pm 90°$ is an indication that tidal effects were inefficient (cf. Fig. 1). Under these assumptions, statistically significant measurements of $\Delta\Phi$ could directly identify how often each of the three formation channels (efficient tides, SMR; efficient tides, RMR; inefficient tides) occurs, for each binary mass.

To illustrate how informative these measurements might be, Fig. 9 shows the relative number of merging binaries that undergo mass-ratio reversal as a function of chirp mass, as derived from the most recent `StarTrack` binary-evolution models [12]. The figure (which is meant to be purely illustrative) refers to Subvariation A of the "standard model" of Dominik et al. [12]. Each panel shows the chirp-mass distribution of binaries that either do (RMR, dashed blue histograms) or do not (SMR, red solid histograms) undergo mass-ratio reversal. This distribution has characteristic "peaks" at specific values of the chirp mass at any given Z and it depends very strongly on composition, as we can see by comparing the two panels (which refer to $Z/Z_\odot = 1$ and $Z/Z_\odot = 0.1$, respectively). According to our model, measurements of $\Delta\Phi$ for a large enough sample of binaries would allow us to reconstruct the shape of these histograms as a function of chirp mass, potentially enabling new high-precision tests of binary evolution, above and beyond the information provided by the mass distribution alone.

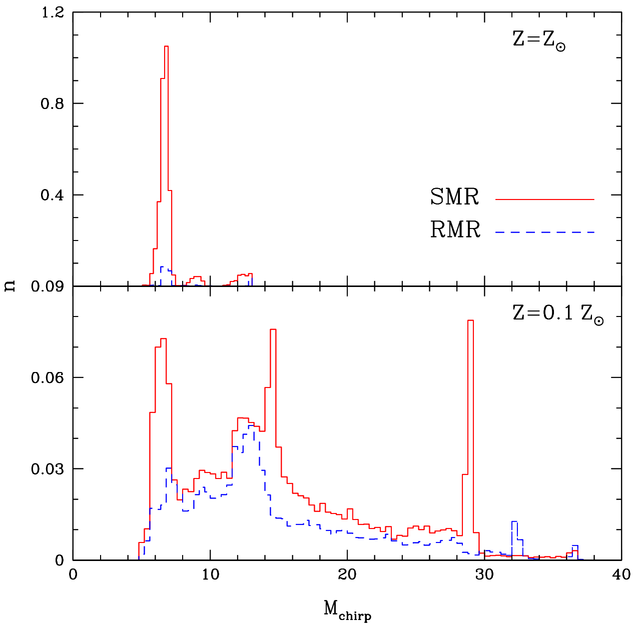

FIG. 9. Histograms of binaries that do (RMR) or do not (SMR) undergo mass-ratio reversal as a function of chirp mass according to the publicly available `StarTrack` data from `http://www.syntheticuniverse.org/`. For illustration, here we choose Subvariation A of the standard model, in the terminology of [12]. A comparison of the upper and lower panels shows the striking differences in the chirp-mass distribution resulting from different choices for the metallicity Z.

A preliminary assessment of the main features of population-synthesis models that could be probed by these measurements can be inferred from Table III. There we list the overall fraction of BH binary systems that undergo mass-ratio reversal for several different binary-evolution scenarios explored in [12]. The most dramatic difference is due to composition: with few exceptions, models with solar composition ($Z/Z_\odot = 1$) almost exclusively produce SMR binaries, while models with subsolar composition ($Z/Z_\odot = 0.1$) produce comparable proportions of SMR and RMR binaries. Furthermore there are clear trends in the ratio RMR/SMR as a function

Variation	Subvariation A $Z/Z_\odot = 0.1$			Subvariation B $Z/Z_\odot = 0.1$			Subvariation A $Z/Z_\odot = 1$			Subvariation B $Z/Z_\odot = 1$		
	SMR	RMR	#	SMR	RMR	#	SMR	RMR	#	SMR	RMR	#
0: Standard	63.2%	36.8%	32496	66.8%	33.2%	17038	91.9%	8.1%	10160	92.9%	7.1%	8795
1: $\lambda = 0.01$	67.9%	32.1%	12368	67.4%	32.6%	11401	93.6%	6.4%	8171	93.6%	6.4%	8171
2: $\lambda = 0.1$	62.7%	37.3%	27698	65.2%	34.8%	16885	88.9%	11.1%	11977	92.1%	7.9%	8577
3: $\lambda = 1$	54.2%	45.8%	51806	65.7%	34.3%	19415	79.1%	20.9%	15820	91.6%	8.4%	8442
4: $\lambda = 10$	50.1%	49.9%	50884	62.9%	37.1%	17939	73.2%	26.8%	14425	91.6%	8.4%	8321
5: $M_{\rm NS} = 3M_\odot$	62.5%	37.5%	32236	66.2%	33.8%	16868	91.6%	8.4%	9972	92.8%	7.2%	8589
6: $M_{\rm NS} = 2M_\odot$	62.3%	37.7%	32535	65.9%	34.1%	16804	91.5%	8.5%	9922	92.5%	7.5%	8590
7: $\sigma = 132.5$km/s	58.2%	41.8%	36546	63.1%	36.9%	18935	88.9%	11.1%	11099	89.6%	10.4%	9334
8: $v_{\rm BH} = v_{\rm pNS}$ (BHs)	56.2%	43.8%	948	72.5%	27.5%	207	56.2%	43.8%	16	0%	100%	2
9: $v_{\rm BH} = 0$ (BHs)	56.3%	43.7%	52832	58.8%	41.2%	34569	66.3%	33.7%	35267	65.2%	34.8%	32547
10: Delayed SN	61.4%	38.6%	27310	66.3%	33.7%	13841	81.5%	18.5%	1032	81.2%	18.8%	881
11: Weak winds	58.4%	41.6%	33872	63.6%	36.4%	17765	70.5%	29.5%	21786	64.2%	35.8%	16182

TABLE III. BH binary rates predicted by `StarTrack`. RMR (SMR) is the percentage of binaries that do (not) experience mass-ratio reversal due to mass transfer; # indicates the total number of BH binaries in the sample. Each row refers to a different variation over the "standard model". The variations illustrate the effect of changing one parameter (CE binding energy λ, kick magnitude, etc.) with respect to the "best guesses" of the standard model. Each row also shows the effect of changing the metallicity Z and the Hertzsprung-gap donor prescription. In Subvariation A (B), binaries can (can not) survive a common-envelope event during the Hertzprung-gap phase; see [12] for details).

of the envelope-binding-energy parameter λ discussed in Appendix A 7 (compare variations 1 to 4); the strength of SN kicks (variations 8 and 9); and the amount of mass loss through winds (variation 11). These parameters are also well known to significantly influence the overall number and mass distribution of merging binaries.

In conclusion, while our model needs further testing and scrutiny against more complete population-synthesis calculations, it strongly indicates that GW measurements of $\Delta\Phi$ and θ_{12} will provide a useful diagnostic of compact binary formation, complementary to the more familiar mass and spin measurements. In the next Section we conclude the paper with an overview of the challenges and rewards associated with these measurements.

V. DISCUSSION

Previous Monte Carlo studies of the spin-orbit resonances discovered by Schnittman [6] showed that spins tend to lock in a resonant plane if the binary has mass ratio $q \gtrsim 0.4$ and the dimensionless spin magnitudes $\chi_i \gtrsim 0.5$ as long as there is an initial asymmetry in the relative orientation of the spins with respect to the orbital angular momentum, i.e. $\theta_1 \neq \theta_2$ [9–11].

In this work we built a toy model for BH binary formation focusing on the main physical ingredients that can produce such an asymmetry: SN kicks (that tilt the orbital plane every time a BH is formed), tidal interactions (that tend to realign the spin of the star that collapses later with the orbital angular momentum) and mass transfer (that can produce mass-ratio reversal, so that the heaviest BH corresponds to the lighter stellar progenitor). We showed that for stellar-mass compact objects formed at the endpoint of isolated binary evolution the required conditions should ubiquitously occur.

Perhaps more interestingly, we demonstrated that the angle $\Delta\Phi$ between the components of the BH spins in the plane orthogonal to the orbital angular momentum is in one-to-one correspondence with the BH formation channel that gave birth to the BH binary: if tides are efficient the PN evolution attracts the spins to the resonant plane with $\Delta\Phi \simeq 0°$ ($\Delta\Phi \simeq \pm 180°$) if mass reversal does (does not) occur. When tidal effects are inefficient the spins precess freely, and they pile up at $\Delta\Phi = \pm 90°$ by the time the binary enters the band of advanced GW detectors. A preliminary comparison with detailed population-synthesis calculations suggests that the fraction of binaries in each family of resonant configurations, both overall and as a function of (chirp) mass, should provide a highly informative diagnostic on some of the main uncertainties involved in binary-evolution physics (metallicity, binding energy of the CE, magnitude of BH kicks). Measuring this fraction will require a large sample of BH mergers with sufficient signal-to-noise ratio, but hopefully such a sample will be obtainable by Advanced LIGO/Virgo after some years of operation at design sensitivity.

Our initial study merits detailed follow-ups to assess (i) the potential accuracy of GW measurements of the precessional parameters, and (ii) the information that can be extracted by comparison with population-synthesis models.

Detailed studies are required from the point of view of GW data analysis. We have assumed for simplicity that each PN resonance can be easily and unambigously distinguished. In practice, accurate matched-filtering measurements of the angles $\Delta\Phi$ and θ_{12} will need more work on the GW source-modeling front. Relevant issues here include the construction of gravitational-waveform templates adapted to resonant configurations, the development of specialized parameter-estimation strategies and the understanding of systematic (as opposed to statistical) errors for second- and third-generation detectors. Spin modulations are known to influence both the amplitude and phase of the emitted radiation, and while there are several preliminary investigations of parameter estimation from spinning, precessing binaries, the direct measurement of parameters characterizing the spin-orbit resonances may require the inclusion of higher-order spin terms and/or higher harmonics in the waveform models.

From an astrophysical standpoint, the observable distribution of binary systems as they enter the detector band should be calculated (more realistically) by applying our PN evolution to initial data derived from state-of-the-art binary population-synthesis models. In addition to corroborating our results, such a study will establish a comprehensive library of reference models that can be compared to observational data using Bayesian or other model-selection strategies: see e.g. [62–68] for previous efforts in this direction. Such a study is necessary also to make contact with other observables, such as as the rate and mass distribution of compact binaries. Only with a comprehensive and self-consistent set of predictions can we quantify how much the information provided by PN resonances complements information available through other observable quantities.

In conclusion, the direct observation of resonant locking will be challenging from a GW data-analysis standpoint. However the relatively transparent astrophysical interpretation of PN resonances makes such an investigation worthwhile. Even if only observationally accessible for the loudest signals, these resonances will enable unique insights into the evolutionary channels that produce merging compact binaries. In our opinion, more detailed studies of resonant locking in connection with population-synthesis models will offer a great observational opportunity for GW astronomy.

ACKNOWLEDGMENTS

We are grateful to Parameswaran Ajith, Chris Belczynski, Tomasz Bulik, Marco Cavaglià, Marc Favata, Or Graur, Michael Horbatsch, Giuseppe Lodato and Sterl Phinney for useful discussions and suggestions on various aspects of this work. This research was supported in part by NSF Grant No. PHY11-25915 and by the LIGO REU program at the California Institute of Technology. ROS was supported by NSF Grant No. PHY-0970074. EB and DG were supported by NSF CAREER Grant No. PHY-1055103. EB and US acknowledge support from FP7-PEOPLE-2011-IRSES Grant No. NRHEP-295189 and NSF-XSEDE Grant No. PHY-090003. US also acknowledges support from FP7-PEOPLE-2011-CIG Grant No. CBHEO-293412, CESGA Grant No. ICTS-234, BSC, RES Grant No. AECT-2012-3-0011, ERC Starting Grant No. DyBHo 256667 and the Cosmos system, part of DiRAC, funded by STFC and BIS.

Appendix A: Binary-evolution phenomenology

Binary population synthesis relies on copious guidance from both observations and theory [69]. Simulations of binary evolution that self-consistently account for stellar structure and mass transfer are computationally expensive and depend on a wide variety of parameters [69, 70]. Models that hope to generate astrophysically realistic binary populations must tabulate the results of these simulations and calibrate them against observations [27, 30, 69]. Well developed algorithms exist to quickly generate large synthetic compact-binary populations similar to those produced in more expensive direct simulations [27, 30]. In this Appendix, we use such population-synthesis models to justify and put into context the simple procedure adopted in this paper. To further validate our model, we have also performed a handful of detailed binary-evolution calculations with the binary-stellar evolution `BSE` code by Hurley et al. [30]. When adopting similar assumptions (i.e., low stellar mass-loss rates and large envelope binding energies), the `BSE` code produces qualitatively similar evolutionary scenarios to the procedure outlined in the text. The simple model and fiducial scenarios considered in this paper do not account for a thorough exploration of the parameter space, but they illustrate the essential physics and demonstrate that PN resonance locking can be the preferred outcome of astrophysically motivated BH binary formation channels.

1. Single stellar evolution

In this Section, we provide relevant information about the evolution of isolated stars. Main-sequence stars born with a mass M_S have a radius [71]

$$\frac{R_S}{R_\odot} \simeq 1.33 \left(\frac{M_S}{M_\odot}\right)^{0.555} . \tag{A1}$$

Massive, metal-rich main-sequence stars lose a substantial amount of mass via winds prior to going SN, but we neglect this mass loss for simplicity. The inclusion of wind mass loss in our model would reduce the mass of the hydrogen envelope available to be transferred to the secondary during the first mass-transfer event. While neglecting this mass loss quantitatively changes the binary evolution, we believe that it does not qualitatively alter our conclusions. Larger (and appropriately chosen) initial stellar masses would lead to final BH binaries with masses comparable to those considered in our model even in the presence of winds.

Stars with main-sequence masses in the range $25\ M_\odot \leq M_S \leq 40\ M_\odot$ evolve into supergiants with helium-core masses well approximated by

$$M_C \simeq 0.1 M_S + 5 M_\odot \tag{A2}$$

(cf. top panel of Fig. 14 of [27]) and radii [72]

$$\frac{R_G}{R_\odot} \simeq 4950 \frac{(M_C/M_\odot)^{4.5}}{1+4(M_C/M_\odot)^4} + 0.5 \ . \tag{A3}$$

Once the hydrogen envelopes have been lost, the naked helium cores have radii [73]

$$\log \frac{R_C}{R_\odot} \simeq -0.699 + 0.0557 \left(\log \frac{M_C}{M_\odot} - 0.172 \right)^{-2.5} . \tag{A4}$$

We neglect further evolution of the naked helium star before SN. For the large masses typical of BH progenitors, the naked helium cores have radiative envelopes and do not expand substantially during subsequent shell burning [27, 74]. After going SN, a main-sequence star leaves behind a BH of mass (bottom panel of Fig. 14 of [27])

$$M_{\rm BH} \simeq 0.3 M_S - 3 M_\odot \ . \tag{A5}$$

2. Initial semimajor axis

The initial binary separation a_0 is drawn from a uniform logarithmic distribution in the range $[a_{\rm min},\, a_{\rm max}]$ [27, 75–77]. The upper limit $a_{\rm max}$ is chosen to ensure that the primary fills its Roche lobe during its supergiant phase, while the lower limit $a_{\rm min}$ is chosen so that the secondary does *not* fill its Roche lobe after receiving mass from the primary. The Roche-lobe radius R_L of a star of mass m_α in an orbit of semimajor axis a about a companion of mass m_β is [30, 78]

$$R_L(a, m_\alpha, m_\beta) \simeq \frac{0.49 Q^{2/3}}{0.6 Q^{2/3} + \ln(1+Q^{1/3})} a \ , \tag{A6}$$

where $Q \equiv m_\alpha/m_\beta$, so the above limits are determined by the constraints

$$R_L(a_{\rm max}, M'_{Si}, M''_{Si}) = R'_G, \tag{A7}$$
$$R_L(a_{\rm min}, M''_{Sf}, M'_C) = R''_{Sf}. \tag{A8}$$

These limits are somewhat arbitrary, but different choices would not affect our main results. In fact, binaries that do not go through mass transfer ($a > a_{\rm max}$) are so widely separated that they are easily unbound by the first SN, while binaries where mass is transferred back to the primary prior to this SN ($a < a_{\rm min}$) will merge in the CE phase. These limits will therefore only affect the failure fractions presented in Table II, not the spin alignments of merging BH binaries.

3. Stable mass transfer

When a star fills its Roche lobe, gas will either be stably transferred to its companion or form a CE about both members of the binary. Stable mass transfer is discussed in this Section of the Appendix, while CE evolution is discussed in Section A 7. In general, the stability of mass transfer depends on the donor star, the accreting star, and the mass ejected to infinity; as a first approximation, stability criteria are usually implemented by simple thresholds on the binary mass ratio, as summarized in [42] and references therein. For our mass ratios, mass transfer from the primary to the secondary prior to the first SN will be stable, while mass transfer from the secondary to the primary between the two SN events will lead to the formation of a CE. A fraction f_a of the mass lost by the primary in the first mass-transfer event will be accreted by the secondary, increasing its mass to

$$M''_{Sf} = M''_{Si} + f_a (M'_{Si} - M'_C) \ . \tag{A9}$$

Fully conservative mass transfer ($f_a = 1$) preserves the total mass of the system, while all of the mass lost by the donor is ejected from the system in fully non-conservative mass transfer ($f_a = 0$). We assume that stable mass transfer is semiconservative ($f_a = 1/2$), in agreement with the standard model of Dominik et al. [12]. Larger values of f_a during this first mass-transfer event will tend to favor the RMR scenario over the SMR scenario. Since f_a is directly tied to the fraction of binaries that undergo mass-ratio reversal in a given mass and mass-ratio range, our model suggests that it is potentially measurable via GW observations. For simplicity, we assume that tides and the mass transfer itself efficiently circularize the orbit (but see [79, 80] for recent investigations of mass transfer and circularization in eccentric binaries).

4. Supernova kicks: magnitude and direction

Following [7], we assume that asymmetric SN events impart hydrodynamical recoils to the newly formed protoneutron stars. We calibrate the magnitude of this primordial kick using observed proper motions of young pulsars: each protoneutron star is kicked with a velocity $v_{\rm pNS}$ drawn from a single Maxwellian with parameter $\sigma = 265$ km/s [81]. A fraction $f_{\rm fb}$ of this asymmetrically ejected material falls back onto the protoneutron star and is accreted as it collapses into a BH. This fallback suppresses the magnitude of the final kick imparted to the BH to $v_{\rm BH} \simeq (1 - f_{\rm fb}) v_{\rm pNS}$; for BHs with masses $M_{\rm BH} = (6 M_\odot, 7.5 M_\odot)$, as in our fiducial scenarios, simulations suggest $f_{\rm fb} \simeq 0.8$ [82, 83]. This BH kick distribution is consistent with the observed proper motions of galactic X-ray binaries hosting BHs [84, 85]. Although our results are not extremely sensitive to the precise magnitude of the BH kicks, the existence of such kicks is crucial to our model, as they are the only observationally well motivated mechanism to introduce misalignment between the compact binary spins and the orbital plane.

We assume that the BH kicks are distributed in a double cone of opening angle θ_b about the BH spin and consider two extreme scenarios: isotropic ($\theta_b = 90°$) or polar ($\theta_b = 10°$) kicks. There is some observational [86, 87] and theoretical [88, 89] support for the polar model. However

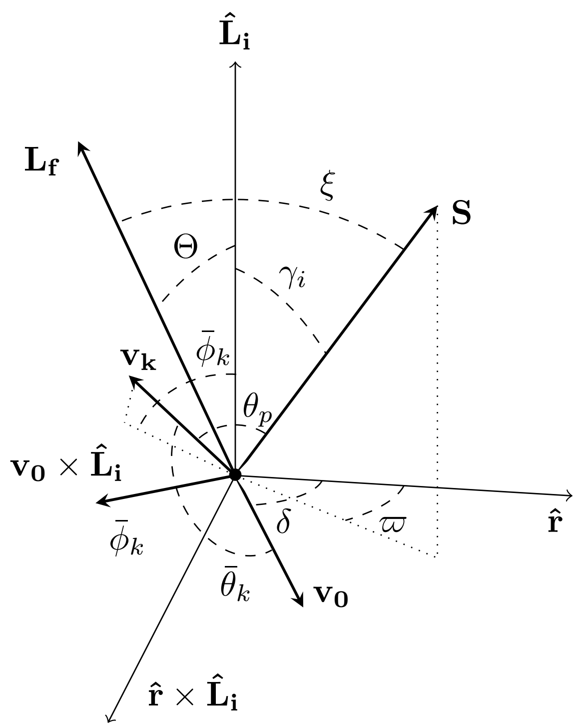

FIG. 10. Definitions of the angles used in Appendix A 5 to study SN kicks. Before the SN, the members of the binary have a separation $\mathbf{r}$ and relative velocity $\mathbf{v_0}$. Mass loss and the SN kick $\mathbf{v_k}$ tilt the orbital angular momentum from $\mathbf{L_i}$ to $\mathbf{L_f}$ while leaving the spin $\mathbf{S}$ unchanged.

we examine both possibilities because this choice has a significant effect on the resulting binary orbits, as discussed in Appendix A 5 below. Our choice of $\theta_b = 10^\circ$ in the polar model was partly motivated by a comparable observed misalignment between the spin and proper motion of the Crab pulsar [56].

5. Supernova kicks: influence on the orbit

In this Section, we describe how SN kicks are implemented in our Monte Carlo calculations. The expressions provided below have been published previously either under more restrictive assumptions [25] or using different notation [30], but we rederive them here for clarity and completeness. Each SN reduces the mass of the binary and imparts a kick to the newly produced compact remnant. We calculate how these effects change the Keplerian orbital elements by applying energy and angular-momentum conservation to the binary before and after the SN. As the duration of the SN explosion is short compared to the other stages of binary evolution, we assume that this orbital modification occurs instantaneously. The definitions of the angles used in this Appendix are illustrated in Fig. 10.

In the simulations reported in this paper we assume that the binary is on a circular orbit ($e_i = 0$) and that the stellar spins are aligned with the orbital angular momentum ($\gamma_i = 0$) when the first SN occurs (we have actually relaxed the circularity assumption in additional simulations not presented here, and we verified that this has a negligible impact on our conclusions). If tides are inefficient, both of these simplifying assumptions will not hold, in general, for the second SN. Therefore here we present general expressions for the post-SN orbital elements. These expression were first derived (to our knowledge) in [30], but here we use notation similar to that of Kalogera [25].

The binary separation r for a Keplerian orbit with initial semimajor axis a_i and eccentricity e_i can be expressed as

$$r = \frac{a_i(1-e_i^2)}{1+e_i\cos\psi_i}, \tag{A10}$$

where ψ_i is the true anomaly. Values for the true anomaly at the time of the SN are chosen by assuming that the explosion is equally likely to occur at any given time. The time t after the binary reaches pericenter is given by

$$\frac{2\pi}{P}t = E - e_i \sin E, \tag{A11}$$

where

$$P = 2\pi\left(\frac{a_i^3}{GM_i}\right)^{1/2} \tag{A12}$$

is the period of a binary of total mass M_i. The eccentric anomaly E is related to the true anomaly ψ_i by

$$\cos\psi_i = \frac{\cos E - e_i}{1 - e_i \cos E}\ . \tag{A13}$$

We assume that t is uniformly distributed in the range $[0, P]$ and derive the corresponding values of ψ_i from these relations.

The direction of the kick velocity $\mathbf{v_k}$ is defined by a polar angle $\bar{\theta}_k$ and an azimuthal angle $\bar{\phi}_k$. Here $\bar{\theta}_k$ is the angle between $\mathbf{v_k}$ and the pre-SN orbital velocity $\mathbf{v_0}$, and the axis defined by $\bar{\phi}_k = 0$ is chosen to be parallel to the orbital angular momentum $\mathbf{L}$ (see Fig. 10). The direction of the spin $\mathbf{S}$ of the collapsing star is specified by the angle γ_i between $\mathbf{S}$ and $\mathbf{L}$ and the angle ϖ between the projection of $\mathbf{S}$ in the orbital plane and the separation $\hat{\mathbf{r}}$ between the members of the binary. In terms of these angles, the angle θ_p between $\mathbf{S}$ and $\mathbf{v_k}$ is given by

$$\begin{aligned}\cos\theta_p = &-\left(\sin\bar{\theta}_k \sin\bar{\phi}_k \sin\delta + \cos\bar{\theta}_k\cos\delta\right)\cos\varpi\sin\gamma_i \\ &+\left(\cos\bar{\theta}_k \sin\delta - \sin\bar{\theta}_k \sin\bar{\phi}_k\cos\delta\right)\sin\varpi\sin\gamma_i \\ &+\sin\bar{\theta}_k\cos\bar{\phi}_k\cos\gamma_i\ ,\end{aligned} \tag{A14}$$

where the angle δ between the orbital velocity and line of separation is given in terms of the true anomaly by

$$\cos\delta = \frac{e_i\sin\psi_i}{\left(1+2e_i\cos\psi_i+e_i^2\right)^{1/2}}\ . \tag{A15}$$

In our Monte Carlo simulations, kick directions are drawn from uniform distributions in $\bar{\phi}_k$, $\cos\bar{\theta}_k$, and ϖ. Kicks confined to within an angle θ_b of the stellar spin $\mathbf{S}$ are therefore implemented by repeated draws from this distribution such that

$$\theta_p \leq \theta_b \qquad \text{or} \qquad \theta_p \geq \pi - \theta_b. \tag{A16}$$

The SN reduces the total mass of the binary from M_i to M_f and changes the velocity of the exploding star from $\mathbf{v_0}$ to $\mathbf{v_0} + \mathbf{v_k}$. Applying energy and angular-momentum conservation to the binary before and after the SN, we find that the final semimajor axis a_f and eccentricity e_f are given by [30]

$$a_f = a_i\,\beta\left[2\,(\beta-1)\,\frac{1+e_i\cos\psi_i}{1-e_i^2} + 1 - u_k^2 - 2u_k\left(\frac{1+2e_i\cos\psi_i+e_i^2}{1-e_i^2}\right)^{1/2}\cos\bar{\theta}_k\right]^{-1}, \tag{A17}$$

$$1-e_f^2 = \frac{1-e_i^2}{\beta^2}\left\{\left[1+u_k\left(\frac{1-e_i^2}{1+2e_i\cos\psi_i+e_i^2}\right)^{1/2}\left(\cos\bar{\theta}_k - \frac{e_i\sin\psi_i\sin\bar{\theta}_k\sin\bar{\phi}_k}{1+e_i\cos\psi_0}\right)\right]^2 + (1-e_i^2)\left(\frac{u_k\sin\bar{\theta}_k\cos\bar{\phi}_k}{1+e_i\cos\psi_i}\right)^2\right\} \times\left[2\,(\beta-1)\,\frac{1+e_i\cos\psi_i}{1-e_i^2} + 1 - u_k^2 - 2u_k\left(\frac{1+2e_i\cos\psi_i+e_i^2}{1-e_i^2}\right)^{1/2}\cos\bar{\theta}_k\right], \tag{A18}$$

where $\beta = M_f/M_i$ and u_k is the magnitude of the kick velocity normalized to the circular orbital velocity before the explosion, i.e.

$$u_k = v_k\sqrt{\frac{a_i}{GM_i}}\,. \tag{A19}$$

If the right-hand side of Eq. (A18) is negative, $e_f > 1$ and the SN has unbound the binary. For binaries that remain bound, the orbital plane is tilted by an angle Θ such that

$$\cos\Theta = \left[1+u_k\left(\frac{1-e_i^2}{1+2e_i\cos\psi_i+e_i^2}\right)^{1/2}\left(\cos\bar{\theta}_k - \frac{e_i\sin\psi_i\sin\bar{\theta}_k\sin\bar{\phi}_k}{1+e_i\cos\psi_i}\right)\right] \times\left\{\left[1+u_k\left(\frac{1-e_i^2}{1+2e_i\cos\psi_i+e_i^2}\right)^{1/2}\left(\cos\bar{\theta}_k - \frac{e_i\sin\psi_i\sin\bar{\theta}_k\sin\bar{\phi}_k}{1+e_i\cos\psi_i}\right)\right]^2 + (1-e_i^2)\left(\frac{u_k\sin\bar{\theta}_k\cos\bar{\phi}_k}{1+e_i\cos\psi_i}\right)^2\right\}^{-1/2}, \tag{A20}$$

and the angle between $\mathbf{S}$ and $\mathbf{L}$ is changed from γ_i to ξ, where

$$\cos\xi = \Bigg\{ \left[1 + u_k \left(\frac{1-e_i^2}{1+2e_i\cos\psi_i + e_i^2} \right)^{1/2} \left(\cos\bar\theta_k - \frac{e_i \sin\psi_i \sin\bar\theta_k \sin\bar\phi_k}{1+e_i\cos\psi_i} \right) \right] \cos\gamma_i - u_k \frac{\sqrt{1-e_i^2}}{1+e_i\cos\psi_i} \sin\bar\theta_k \cos\bar\phi_k \sin\gamma_i \sin\varpi \Bigg\} \times \Bigg\{ \left[1 + u_k \left(\frac{1-e_i^2}{1+2e_i\cos\psi_i + e_i^2} \right)^{1/2} \left(\cos\bar\theta_k - \frac{e_i \sin\psi_i \sin\bar\theta_k \sin\bar\phi_k}{1+e_i\cos\psi_i} \right) \right]^2 + (1-e_i^2) \left(\frac{u_k \sin\bar\theta_k \cos\bar\phi_k}{1+e_i\cos\psi_i} \right)^2 \Bigg\}^{-1/2} . \tag{A21}$$

When $\mathbf{S}$ is aligned with $\mathbf{L}$ before the SN ($\gamma_i = 0$), the tilt of the orbital plane equals the misalignment of the exploding star's spin ($\xi = \Theta$).

The above expressions greatly simplify for initially circular binaries. For example, the SN will disrupt the binary if

$$u_k^2 + 2u_k \cos\bar\theta_k + 1 - 2\beta > 0 \quad (e_i = 0)\,. \tag{A22}$$

The equations simplify even further if $\mathbf{S}$ and $\mathbf{L}$ are initially aligned ($\gamma_i = 0$), in which case exactly polar kicks are given by $\bar\theta_k = \pi/2, \bar\phi_k = 0$. Exactly polar kicks larger than $u_k > \sqrt{2\beta - 1}$ always unbind the binary, while for isotropic kicks a bound tail of the distribution remains provided $u_k < 1 + \sqrt{2\beta}$. If kicks are confined to cones within an angle θ_b of $\mathbf{L}$, the minimum final semimajor axis is

$$a_{f,\mathrm{Min}} = \frac{a_i \beta}{2\beta - \cos^2\theta_b} \quad (e_i = 0, \gamma_i = 0)\;; \tag{A23}$$

exactly polar kicks ($\theta_b = 0$) can only increase the semimajor axis ($a_{f,\mathrm{Min}} > a_1$), while isotropic kicks ($\theta_b = 90°$) can reduce the semimajor axis by at most a factor of 2 ($a_{f,\mathrm{Min}} = a_1/2$).

Exactly polar kicks also add a significant component of angular momentum perpendicular to the initial orbital plane, leading to a strong spin tilt:

$$\cos\Theta = \frac{1}{\sqrt{1+u_k^2}} \quad (e_i = 0, \gamma_i = 0)\,. \tag{A24}$$

However, the maximum tilt that polar kicks can produce while the binary remains bound is

$$\Theta = \cos^{-1}(2\beta)^{-1/2}\,. \tag{A25}$$

By contrast, isotropic kicks can make the binary more tightly bound, allowing greater latitude for kicks to produce bound systems with large spin misalignments.

In the limit that the kick velocity is small compared to the orbital velocity ($u_k \ll 1$), as should be the case for the second SN after CE evolution has reduced the binary separation, the tilt of the orbital plane is given by

$$\Theta = u_k \sin\bar\theta_k |\cos\bar\phi_k| + \mathcal{O}(u_k^{3/2}) \quad (e_i = 0, \gamma_i = 0)\,. \tag{A26}$$

6. Tidal alignment

As discussed in Sec. II B, tidal dissipation can circularize the orbit of the binary and align the spin of the secondary with the orbital angular momentum between the two SN explosions [30, 90, 91]. A detailed treatment of the theory of tidal damping in massive stars is far beyond the scope of this paper, and relatively little data exists to calibrate these theoretical models if we wished to do so. We therefore only consider the two extreme possibilities: tides can either fully circularize the binary and align the spin of the secondary, or they are completely inefficient. We provide order-of-magnitude estimates for tidal processes below; those interested in more details should consult one of the several excellent published reviews of tidal processes [69, 91, 92].

Tides should generally act on both members of the binary. However tidal effects on the BH can safely be ignored, given its small size. We therefore focus on tidal effects on the secondary between the two SN (phase **d** of the evolutionary scenario presented in Fig. 3). If the secondary is fully convective, as expected for the core of a BH progenitor, convection causes internal damping on the viscous timescale $t_V \simeq \gamma^{-1}(3M_S R_S^2/L_S)^{1/3}$, where M_S, R_S and L_S are the mass, radius and luminosity of the secondary, and γ is a prefactor that depends on details of the stellar structure [92]. The orbit evolves on the tidal-friction timescale

$$t_{\rm tid} \simeq \tilde{k}\, \frac{t_V}{9} \frac{M_{\rm S}^2}{(M_{\rm BH}+M_S)M_{\rm BH}} \left(\frac{a}{R_S}\right)^8 \simeq 4\times 10^{-3}\, \tilde{k}\gamma\, \frac{1}{Q(1+Q)} \left(\frac{M_{\rm S}}{10M_\odot}\right)^{1/3} \left(\frac{R_{\rm S}}{10R_\odot}\right)^{2/3} \times \left(\frac{L_{\rm S}}{10^4 L_\odot}\right)^{-1/3} \left(\frac{a}{R_{\rm S}}\right)^8 \mathrm{yrs}, \tag{A27}$$

where $M_{\rm BH}$ is the mass of the primary, $Q = M_{\rm BH}/M_S$ is the mass ratio at this stage of the evolution, and $\tilde{k}\gamma$ is a constant of order unity depending on the internal structure of the star [91]. Though the details depend on the initial stellar spin, tidal friction should synchronize and align the spin of the secondary with the now circular orbit on this same short timescale [92].

The most notable feature of the tidal-friction timescale $t_{\rm tid}$ given by Eq. (A27) is its extremely steep dependence on the ratio a/R_S. While the secondary remains on the main sequence with a radius given by Eq. (A1), this ratio is typically 100 or greater for binaries that avoid merging during CE evolution. This implies that tidal alignment occurs on timescales much longer than the Hubble time $t_H \simeq 10^{10}$ yrs. However, once the secondary evolves to fill its Roche lobe, its radius is given by Eq. (A6) and the ratio a/R_S becomes of order unity. This reduces the tidal-friction timescale well below typical stellar-evolution timescales of a few million years (hydrogen-core burning) or even the briefer time

$$t_{\rm HG} \simeq 2.7 \times 10^4 \left(\frac{M_{\rm C}}{10M_\odot}\right)^2 \left(\frac{R_{\rm C}}{10R_\odot}\right)^{-1} \left(\frac{L_{\rm S}}{10^4L_\odot}\right)^{-1} {\rm yrs} \tag{A28}$$

that the secondary spends on the Hertzsprung gap after exhausting the hydrogen in its core (i.e., the Kelvin-Helmholtz timescale of the core). Since our fiducial scenarios require the secondary to fill its Roche lobe prior to the second SN, one might expect tidal alignment to always be efficient. Substantial uncertainties remain in the model however. Stars with partially radiative envelopes may have longer tidal-friction timescales [27, 69], and the stellar core may not efficiently couple to its envelope, as suggested by recent Kepler observations of core-rotation rates [93]. Therefore, for completeness, we also explore the "extreme" alternative scenario of completely inefficient tidal alignment.

Being dissipative in nature, tidal interactions decrease the semimajor axis in addition to circularizing the orbit. This change is small compared to that induced by CE evolution, as discussed in the next Section, and can therefore be neglected along with the orbital changes produced by other phenomena (e.g. magnetic braking and mass transfer).

7. Common-envelope evolution

If the semimajor axis a_1 of the binary following the first SN is greater than $a_{\rm noCE}$, as determined from the constraint

$$R_L(a_{\rm noCE}, M''_{Sf}, M'_{\rm BH}) = R''_G \tag{A29}$$

with R''_G given by Eq. (A3), the secondary does not fill its Roche lobe and no CE evolution occurs. For smaller values of a_1, we use conservation of energy to determine how much the binary's orbit shrinks during CE evolution. The gravitational binding energy of the CE can be expressed as

$$E_b = -\frac{GM''_{Sf}\left(M''_{Sf} - M''_C\right)}{\lambda\mathcal{R}} \ , \tag{A30}$$

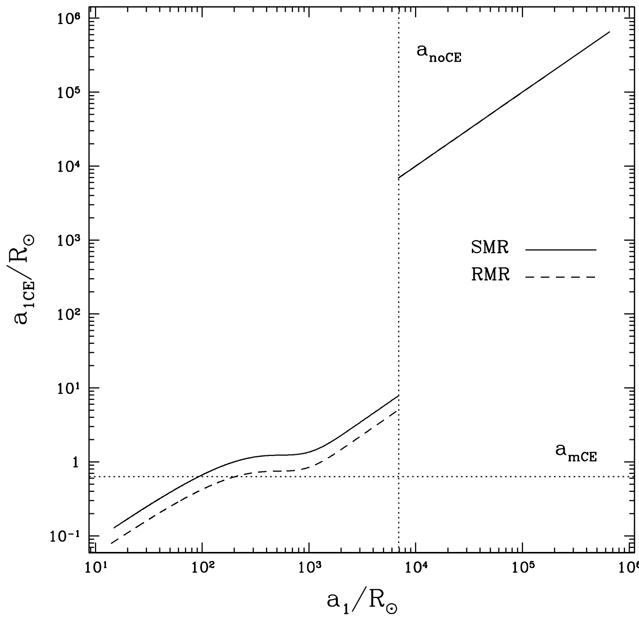

FIG. 11. The semimajor axis a_{1CE} at the end of CE evolution as a function of its initial value a_1 in both the SMR and RMR scenarios. If $a_1 > a_{\rm noCE}$, as given implicitly by Eq. (A29), the secondary fails to fill its Roche lobe, no CE evolution occurs, and $a_{1CE} = a_1$. If $a_{1CE} < a_{\rm mCE}$, as given implicitly by Eq. (A34), the helium core of the secondary fills its Roche lobe prior to the end of CE and the binary merges, failing to eventually form a BH binary. The nonlinear relationship between pre- and post-CE semimajor axes when $a_1 < a_{\rm noCE}$ results from the nontrivial dependence of the CE efficiency parameter λ on a_1, as given by Eq. (A31).

where M''_{Sf} is the mass of the secondary at the onset of CE evolution, $M''_{Sf} - M''_C$ is the mass lost by the secondary during this evolution, $\mathcal{R} = R_L(a_1, M''_{Sf}, M'_{\rm BH})$ is the Roche-lobe radius of the secondary at the onset of CE evolution, and λ is a dimensionless parameter of order unity that depends on the mass and structure of the secondary, notably the location of the core-envelope boundary. Full stellar-evolution codes can be used to calculate the appropriate value of λ for our BH progenitors [94–96]. We adopt an analytic fit to Fig. 3 of [12], which summarizes the results of these calculations:

$$\lambda = ae^{-b\,\mathcal{R}/R_\odot} + c \ , \tag{A31}$$

where $a = 0.358$, $b = 7.19 \times 10^{-3}$, and $c = 0.05$. Conservation of energy during CE evolution implies

$$-\frac{GM'_{\rm BH}M''_{Sf}}{2a_1} + E_b = -\frac{GM'_{\rm BH}M''_C}{2a_{1CE}} \ ; \tag{A32}$$

solving for a_{1CE} yields

$$a_{1CE} = a_1 \frac{M''_{\rm C}}{M''_{\rm Sf}} \left(1 + \frac{2}{\lambda}\frac{a_1}{\mathcal{R}}\frac{M''_{\rm Sf} - M''_{\rm C}}{M'_{\rm BH}}\right)^{-1} \ . \tag{A33}$$

If a_{1CE} is less than a_{mCE}, as determined from the constraint

$$R_L(a_{\mathrm{mCE}}, M_C'', M_{\mathrm{BH}}') = R_C'' \tag{A34}$$

with R_C'' given by Eq. (A4), the helium core of the secondary itself fills its Roche lobe before the end of CE evolution. This leads to a prompt merger, preventing the eventual formation of a BH binary. Our final prescription for a_{1CE} as a function of a_1 is shown in Fig. 11. CE evolution is crucial to our model, shrinking the semimajor axis by a factor $\sim 10^3$ and thereby allowing the eventual BH binary to merge in less than a Hubble time.

Motivated by hydrodynamical simulations [97, 98] and previous work on binary evolution, we neglect accretion onto the primary BH during CE evolution. These studies suggest that the BH accretes at substantially less than the Bondi-Hoyle rate during the evolution, accumulating $\lesssim 0.1 M_\odot$ in mass. Given this small change in mass, we are justified in ignoring any resulting changes in the BH spin [99]. As noted in Appendix A 1, we also neglect the expansion of naked helium stars, and therefore explicitly forbid a helium-star CE phase [74].

[1] G. M. Harry and the LIGO Scientific Collaboration, Class. Quantum Grav. **27**, 084006 (2010).
[2] IndIGO webpage, `http://www.gw-indigo.org/` (2012).
[3] K. Somiya (KAGRA Collaboration), Class.Quant.Grav. **29**, 124007 (2012), arXiv:1111.7185 [gr-qc].
[4] M. Punturo *et al.*, Class. Quantum Grav. **27**, 194002 (2010).
[5] B. Sathyaprakash and B. Schutz, Living Rev.Rel. **12**, 2 (2009), arXiv:0903.0338 [gr-qc].
[6] J. D. Schnittman, Phys. Rev. D **70**, 124020 (2004), arXiv:astro-ph/0409174.
[7] K. Belczynski, R. E. Taam, E. Rantsiou, and M. van der Sluys, Astrophys.J. **682**, 474 (2008), arXiv:astro-ph/0703131.
[8] T. Fragos, M. Tremmel, E. Rantsiou, and K. Belczynski, Astrophys.J. **719**, L79 (2010), arXiv:1001.1107 [astro-ph.HE].
[9] M. Kesden, U. Sperhake, and E. Berti, Phys. Rev. D **81**, 084054 (2010), arXiv:1002.2643 [astro-ph.GA].
[10] M. Kesden, U. Sperhake, and E. Berti, Astrophys.J. **715**, 1006 (2010), arXiv:1003.4993 [astro-ph.CO].
[11] E. Berti, M. Kesden, and U. Sperhake, Phys. Rev. D **85**, 124049 (2012), arXiv:1203.2920 [astro-ph.HE].
[12] M. Dominik, K. Belczynski, C. Fryer, D. E. Holz, E. Berti, T. Bulik, I. Mandel, and R. O'Shaughnessy, Astrophys.J. **759**, 52 (2012), arXiv:1202.4901 [astro-ph.HE].
[13] T. Bogdanović, C. S. Reynolds, and M. C. Miller, Astrophys.J. **661**, L147 (2007), arXiv:astro-ph/0703054.
[14] E. Berti, V. Cardoso, and A. O. Starinets, Classical and Quantum Gravity **26**, 163001 (2009), arXiv:0905.2975 [gr-qc].
[15] J. F. Steiner, J. E. McClintock, and R. Narayan, ApJ **762**, 104 (2013), arXiv:1211.5379 [astro-ph.HE].
[16] G. B. Cook, S. L. Shapiro, and S. A. Teukolsky, Astrophys.J. **424**, 823 (1994).
[17] E. Berti and N. Stergioulas, Mon.Not.Roy.Astron.Soc. **350**, 1416 (2004), arXiv:gr-qc/0310061 [gr-qc].
[18] K.-W. Lo and L.-M. Lin, Astrophys.J. **728**, 12 (2011), arXiv:1011.3563 [astro-ph.HE].
[19] I. Mandel and R. O'Shaughnessy, Class.Quant.Grav. **27**, 114007 (2010), arXiv:0912.1074 [astro-ph.HE].
[20] D. A. Brown, I. Harry, A. Lundgren, and A. H. Nitz, Phys.Rev. **D86**, 084017 (2012), arXiv:1207.6406 [gr-qc].
[21] D. R. Lorimer, Living Reviews in Relativity **4** (2001), 10.12942/lrr-2001-5.
[22] D. Chakrabarty, in *American Institute of Physics Conference Series*, American Institute of Physics Conference Series, Vol. 1068, edited by R. Wijnands, D. Altamirano, P. Soleri, N. Degenaar, N. Rea, P. Casella, A. Patruno, and M. Linares (2008) pp. 67–74, arXiv:0809.4031.
[23] J. W. Hessels, S. M. Ransom, I. H. Stairs, P. C. C. Freire, V. M. Kaspi, *et al.*, Science **311**, 1901 (2006), arXiv:astro-ph/0601337 [astro-ph].
[24] M. Burgay, N. D'Amico, A. Possenti, R. Manchester, A. Lyne, *et al.*, Nature **426**, 531 (2003), arXiv:astro-ph/0312071 [astro-ph].
[25] V. Kalogera, Astrophys.J. **541**, 319 (2000), arXiv:astro-ph/9911417.
[26] K. Belczynski, V. Kalogera, and T. Bulik, Astrophys.J. **572**, 407 (2002), arXiv:astro-ph/0111452.
[27] K. Belczynski, V. Kalogera, F. A. Rasio, R. E. Taam, A. Zezas, T. Bulik, T. J. Maccarone, and N. Ivanova, Astrophys.J.s **174**, 223 (2008), arXiv:astro-ph/0511811.
[28] K. Belczynski, G. Wiktorowicz, C. L. Fryer, D. E. Holz, and V. Kalogera, Astrophys.J. **757**, 91 (2012), arXiv:1110.1635 [astro-ph.GA].
[29] J. R. Hurley, O. R. Pols, and C. A. Tout, MNRAS **315**, 543 (2000), arXiv:astro-ph/0001295.
[30] J. R. Hurley, C. A. Tout, and O. R. Pols, MNRAS **329**, 897 (2002), arXiv:astro-ph/0201220.
[31] R. W. O'Shaughnessy, J. Kaplan, V. Kalogera, and K. Belczynski, Astrophys.J. **632**, 1035 (2005), arXiv:astro-ph/0503219 [astro-ph].
[32] P. C. Peters, Physical Review **136**, 1224 (1964).
[33] P. C. Peters and J. Mathews, Physical Review **131**, 435 (1963).
[34] R. A. Rossiter, ApJ **60**, 15 (1924).
[35] D. B. McLaughlin, ApJ **60**, 22 (1924).
[36] S. Albrecht, S. Reffert, I. Snellen, A. Quirrenbach, and D. S. Mitchell, A&A **474**, 565 (2007), arXiv:0708.2918.
[37] S. Albrecht, J. N. Winn, J. A. Carter, I. A. G. Snellen, and E. J. W. de Mooij, ApJ **726**, 68 (2011), arXiv:1011.0425 [astro-ph.SR].
[38] S. Albrecht, J. Setiawan, G. Torres, D. C. Fabrycky, and J. N. Winn, ArXiv e-prints (2012), arXiv:1211.7065 [astro-ph.SR].
[39] S. Albrecht, S. Reffert, I. A. G. Snellen, and J. N. Winn, Nature **461**, 373 (2009), arXiv:0909.2861 [astro-ph.SR].
[40] G. E. Soberman, E. S. Phinney, and E. P. J. van den Heuvel, Astron.&Astrophys. **327**, 620 (1997), arXiv:astro-ph/9703016.
[41] H. Ge, R. F. Webbink, Z. Han, and X. Chen, Ap&SS **329**, 243 (2010), arXiv:1005.3105 [astro-ph.SR].
[42] D. Clausen, R. A. Wade, R. K. Kopparapu, and R. O'Shaughnessy, Astrophys.J. **746**, 186 (2012), arXiv:1201.0012 [astro-ph.SR].
[43] P. Peters and J. Mathews, Phys.Rev. **131**, 435 (1963).
[44] K. Belczynski and M. Dominik, ArXiv e-prints (2012), arXiv:1208.0358 [astro-ph.HE].
[45] K. A. Postnov and A. G. Kuranov, MNRAS **384**, 1393 (2008), arXiv:0710.4465.
[46] L. Blanchet, Living Reviews in Relativity **5**, 3 (2002), arXiv:gr-qc/0202016.
[47] N. Yunes and E. Berti, Phys.Rev. **D77**, 124006 (2008), arXiv:0803.1853 [gr-qc].
[48] A. Buonanno, B. R. Iyer, E. Ochsner, Y. Pan, and B. S. Sathyaprakash, Phys. Rev. D **80**, 084043 (2009), arXiv:0907.0700 [gr-qc].
[49] Z. Zhang, N. Yunes, and E. Berti, Phys.Rev. **D84**, 024029 (2011), arXiv:1103.6041 [gr-qc].
[50] L. E. Kidder, Phys. Rev. D **52**, 821 (1995), arXiv:gr-qc/9506022.
[51] K. G. Arun, A. Buonanno, G. Faye, and E. Ochsner, Phys. Rev. D **79**, 104023 (2009).
[52] K. G. Arun, A. Buonanno, G. Faye, and E. Ochsner, Phys. Rev. D **84**, 049901 (2011).
[53] P. Ajith and M. Favata, in preparation (2013).
[54] T. Damour, Phys. Rev. D **64**, 124013 (2001), arXiv:gr-qc/0103018.
[55] W. H. Press, S. A. Teukolsky, W. T. Vetterling, and B. P. Flannery, *Numerical recipes in C++ : the art of*

scientific computing by William H. Press. xxviii, 1,002 p. : ill. ; 26 cm. Includes bibliographical references and index. ISBN : 0521750334 (2002).
[56] D. L. Kaplan, S. Chatterjee, B. M. Gaensler, and J. Anderson, Astrophys.J. **677**, 1201 (2008), arXiv:0801.1142.
[57] M. Ugliano, H.-T. Janka, A. Marek, and A. Arcones, Astrophys.J. **757**, 69 (2012), arXiv:1205.3657 [astro-ph.SR].
[58] E. O'Connor and C. D. Ott, ApJ **730**, 70 (2011), arXiv:1010.5550 [astro-ph.HE].
[59] W. M. Farr, K. Kremer, M. Lyutikov, and V. Kalogera, Astrophys.J. **742**, 81 (2011), arXiv:1104.5001 [astro-ph.HE].
[60] C. Cutler and E. E. Flanagan, Phys.Rev. **D49**, 2658 (1994), arXiv:gr-qc/9402014 [gr-qc].
[61] E. Poisson and C. M. Will, Phys.Rev. **D52**, 848 (1995), arXiv:gr-qc/9502040 [gr-qc].
[62] I. Mandel and R. O'Shaughnessy, Classical and Quantum Gravity **27**, 114007 (2010), arXiv:0912.1074 [astro-ph.HE].
[63] R. W. O'Shaughnessy, C. Kim, V. Kalogera, and K. Belczynski, Astrophys.J. **672**, 479 (2008), arXiv:astro-ph/0610076 [astro-ph].
[64] R. O'Shaughnessy, V. Kalogera, and K. Belczynski, Astrophys.J. **716**, 615 (2010), arXiv:0908.3635 [astro-ph.CO].
[65] I. Mandel, Phys.Rev. **D81**, 084029 (2010), arXiv:0912.5531 [astro-ph.HE].
[66] A. Sesana, J. Gair, E. Berti, and M. Volonteri, Phys.Rev. **D83**, 044036 (2011), arXiv:1011.5893 [astro-ph.CO].
[67] J. R. Gair, A. Sesana, E. Berti, and M. Volonteri, Class.Quant.Grav. **28**, 094018 (2011), arXiv:1009.6172 [gr-qc].
[68] R. O'Shaughnessy, (2012), arXiv:1204.3117 [astro-ph.CO].
[69] P. Eggleton, *Evolutionary Processes in Binary and Multiple Stars, by Peter Eggleton, pp. . ISBN 0521855578. Cambridge, UK: Cambridge University Press, 2006.* (2006).
[70] B. Paxton, L. Bildsten, A. Dotter, F. Herwig, P. Lesaffre, and F. Timmes, (arXiv:1009.1622) (2010).
[71] O. Demircan and G. Kahraman, Ap&SS **181**, 313 (1991).
[72] S. Rappaport, P. Podsiadlowski, P. C. Joss, R. Di Stefano, and Z. Han, MNRAS **273**, 731 (1995).
[73] C. L. Fryer and S. E. Woosley, Astrophys.J. **502**, L9 (1998), arXiv:astro-ph/9804167.
[74] N. Ivanova, K. Belczynski, V. Kalogera, F. A. Rasio, and R. E. Taam, Astrophys.J. **592**, 475 (2003), arXiv:astro-ph/0210267.
[75] E. Öpik, Publications of the Tartu Astrofizica Observatory **25**, 1 (1924).
[76] H. A. Abt, ARA&A **21**, 343 (1983).
[77] A. Poveda, C. Allen, and A. Hernández-Alcántara, in *IAU Symposium*, IAU Symposium, Vol. 240, edited by W. I. Hartkopf, P. Harmanec, and E. F. Guinan (2007) pp. 417–425, arXiv:0705.2021.
[78] P. P. Eggleton, Astrophys.J. **268**, 368 (1983).
[79] J. F. Sepinsky, B. Willems, V. Kalogera, and F. A. Rasio, Astrophys.J. **702**, 1387 (2009), arXiv:0903.0621 [astro-ph.SR].
[80] J. F. Sepinsky, B. Willems, V. Kalogera, and F. A. Rasio, Astrophys.J. **724**, 546 (2010), arXiv:1005.0625 [astro-ph.SR].
[81] G. Hobbs, D. R. Lorimer, A. G. Lyne, and M. Kramer, MNRAS **360**, 974 (2005), arXiv:astro-ph/0504584.
[82] C. L. Fryer, Astrophys.J. **522**, 413 (1999), arXiv:astro-ph/9902315.
[83] C. L. Fryer and V. Kalogera, Astrophys.J. **554**, 548 (2001), arXiv:astro-ph/9911312.
[84] T. Fragos, B. Willems, V. Kalogera, N. Ivanova, G. Rockefeller, C. L. Fryer, and P. A. Young, Astrophys.J. **697**, 1057 (2009), arXiv:0809.1588.
[85] T.-W. Wong, F. Valsecchi, T. Fragos, and V. Kalogera, Astrophys.J. **747**, 111 (2012), arXiv:1107.5585 [astro-ph.HE].
[86] C. Wang, D. Lai, and J. L. Han, Astrophys.J. **639**, 1007 (2006), arXiv:astro-ph/0509484.
[87] A. Noutsos, D. Schnitzeler, E. Keane, M. Kramer, and S. Johnston, (arXiv:1301.1265) (2013).
[88] H. Spruit and E. S. Phinney, Nature **393**, 139 (1998), arXiv:astro-ph/9803201.
[89] D. Lai, D. F. Chernoff, and J. M. Cordes, Astrophys.J. **549**, 1111 (2001), arXiv:astro-ph/0007272.
[90] J.-P. Zahn, Astron.&Astrophys. **41**, 329 (1975).
[91] P. Hut, Astron.&Astrophys. **99**, 126 (1981).
[92] P. P. Eggleton and L. Kiseleva-Eggleton, Astrophys.J. **562**, 1012 (2001), arXiv:astro-ph/0104126.
[93] P. G. Beck, J. Montalban, T. Kallinger, J. De Ridder, C. Aerts, R. A. García, S. Hekker, M.-A. Dupret, B. Mosser, P. Eggenberger, D. Stello, Y. Elsworth, S. Frandsen, F. Carrier, M. Hillen, M. Gruberbauer, J. Christensen-Dalsgaard, A. Miglio, M. Valentini, T. R. Bedding, H. Kjeldsen, F. R. Girouard, J. R. Hall, and K. A. Ibrahim, Nature **481**, 55 (2012), arXiv:1112.2825 [astro-ph.SR].
[94] X.-J. Xu and X.-D. Li, Astrophys.J. **716**, 114 (2010), arXiv:1004.4957 [astro-ph.SR].
[95] X.-J. Xu and X.-D. Li, Astrophys.J. **722**, 1985 (2010).
[96] A. J. Loveridge, M. V. van der Sluys, and V. Kalogera, Astrophys.J. **743**, 49 (2011), arXiv:1009.5400 [astro-ph.SR].
[97] P. M. Ricker and R. E. Taam, Astrophys.J. **672**, L41 (2008), arXiv:0710.3631.
[98] P. M. Ricker and R. E. Taam, Astrophys.J. **746**, 74 (2012), arXiv:1107.3889 [astro-ph.SR].
[99] A. R. King and U. Kolb, MNRAS **305**, 654 (1999), arXiv:astro-ph/9901296.